KLOE Note n. 221

Measurement of the $\sigma(e^+e^- \to \pi^+\pi^-\gamma(\gamma))$ and the dipion contribution to the muon anomaly with the KLOE detector

Stefan Müller[a], Federico Nguyen[b], Graziano Venanzoni[a], Paolo Beltrame[d], Achim Denig[d], Wolfgang Kluge[c]

[a] *Laboratori Nazionali di Frascati dell'INFN, Frascati, Italy*
[b] *Dipartimento di Fisica dell'Università "Roma Tre" e Sezione INFN, Rome, Italy*
[c] *Institut für Experimentelle Kernphysik, Universität Karlsruhe, Germany*
[d] *Institut für Kernphysik, Universität Mainz, Germany*

23rd September 2008

Abstract

We have measured the cross section $\sigma(e^+e^- \to \pi^+\pi^-\gamma(\gamma))$ at DAΦNE, the Frascati ϕ–factory, using events with initial state radiation photons emitted at small angle and inclusive of final state radiation. We present the analysis of a new data set corresponding to an integrated luminosity of 240 pb^{-1}. We have achieved a reduced systematic uncertainty with respect to previously published KLOE results. From the cross section we obtain the pion form factor and the contribution to the muon magnetic anomaly from two-pion states in the mass range $0.592 < M_{\pi\pi} < 0.975$ GeV. For the latter we find $\Delta^{\pi\pi}a_\mu=(387.2\pm0.5_{\rm stat}\pm2.4_{\rm exp}\pm2.3_{\rm th})\times10^{-10}$.

Contents

1 Introduction

The muon magnetic anomaly, a_μ, has been recently measured at Brookhaven with an accuracy of 0.54 ppm [1]. The value of a_μ in the standard model, is found to differ from the experimental value by 2.8 to 3.4 standard deviations [2,3]. The main source of uncertainty in the estimate of a_μ is the hadronic contribution, which is not calculable in perturbative QCD. The hadronic contribution, at lowest order, $\Delta^{\mathrm{h,lo}}a_\mu$, is obtained from a dispersive integral over the cross section for $e^+e^-\to$hadrons [4,5]. The $e^+e^-\to\pi^+\pi^-$ channel accounts for $\sim 70\%$ of $\Delta^{\mathrm{h,lo}}a_\mu$ and $\sim 60\%$ of its uncertainty.

It should be noted that the physically measurable cross section for $e^+e^-\to\pi^+\pi^-$ as such, cannot be used in the dispersive integral for two reasons. The first, obviously, is that the measured cross section is affected by initial state radiation (ISR) which must not be included in the contribution to the muon anomaly. Even the energy at the $\pi\pi\gamma$ vertex is different from the nominal e^+e^- collision energy. The second reason is more a question of tradition and book keeping. The photon at the $\pi^+\pi^-\gamma$ vertex, at lowest order, is a bare photon, *i.e.* without vacuum polarization. The measured cross section must be therefore corrected for both effects, as we discuss later. Final state radiation (FSR) from the pions must instead be included. The measured quantities therefore require corrections for the photon vacuum polarization, for ISR, and to ensure that pion FSR is included, since some of the events with FSR might have been rejected. In our measurement there are some additional corrections, mostly due to ambiguities between ISR and FSR because we measure the dipion mass and not the e^+e^- collision energy.

In 2005, we published [6] a measurement of the dipion contribution $\Delta^{\pi\pi}a_\mu$, using the method described in Sec. 2, using data collected in 2001 for $\int\mathcal{L}\mathrm{d}t$=140 pb^{-1}, with a fractional systematic error of 1.3%. We discuss in the following a new and more accurate measurement of the same quantity.

In particular, the following changes are applied with respect to the data taken in 2001:

- an additional third level trigger was implemented during 2002 to reduce the inefficiency on the signal $\pi^+\pi^-\gamma$ events due to the KLOE detector's cosmic ray muon trigger-veto, bringing this inefficiency down to few per mill. This has to be compared with the trigger condition during 2001 data taking, in which the signal efficiency was reduced by as much as 30% due to the misidentification of pions as cosmic ray events,

- an improved offline background filter was used with the new data sample. This filter contributed the largest experimental systematic uncertainty to the published analysis. A downscaling algorithm providing an unbiased control sample allows the evaluation of the filter efficiency with negligible systematic uncertainty,

- The requirement to have the two tracks form a vertex has been dropped. The vertex efficiency introduced a 0.3% uncertainty in the previous analysis [6].

In addition, the knowledge of the detector response and of the KLOE simulation program have been improved [7].

2 Measurement of $e^+e^- \to \pi^+\pi^-$ cross section at DAΦNE

The KLOE detector operates at DAΦNE, the Frascati ϕ–factory, a "small angle" e^+e^- collider running mainly at a center of mass energy equal to the ϕ meson mass, $W{\sim}1020$ MeV. At DAΦNE, we measure the differential cross section for $e^+e^- \to \pi^+\pi^-\gamma$ as a function of the $\pi^+\pi^-$ invariant mass, $M_{\pi\pi}$, for ISR events, and obtain the dipion cross section $\sigma_{\pi\pi} \equiv \sigma(e^+e^- \to \pi^+\pi^-)$ from [8]:

$$s \left.\frac{\mathrm{d}\sigma(ee \to \pi\pi\gamma)}{\mathrm{d}M^2_{\pi\pi}}\right|_{\mathrm{ISR}} = \sigma_{\pi\pi}(M^2_{\pi\pi})\ H(M^2_{\pi\pi}, s). \tag{2.1}$$

Eq. 2.1 defines H, the "radiator function". H can be obtained from QED calculations and depends on the e^+e^- center of mass energy squared s. In eq. 2.1 we neglect FSR, which however is included in our analysis. The cross section we obtain is inclusive of all radiation in the final state.

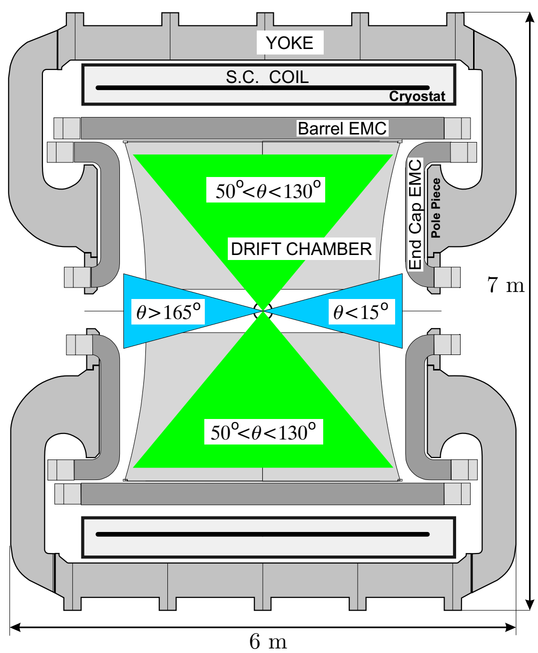

Figure 1: Vertical cross section of the KLOE detector, showing the small and large angle regions where photons and pions are accepted

3 Event selection

3.1 Preselection

The data sample consists of $\int\mathcal{L}\mathrm{d}t$=240 pb^{-1} of data taken in the year 2002, which have been preselected by a streaming algorithm using the following cuts:

- at least 2 charged tracks with opposite charge crossing a cylinder centered around the beam interaction point (IP) with 30 cm length and 8 cm radius

- at least one pair of two tracks must satisfy:

  - 150 MeV $< |\vec{p}_1| + |\vec{p}_2| <$ 1020 MeV
  - ($-$220 MeV) $< M_{\text{Miss}} <$ 120 MeV
  - 80 MeV $< M_{\text{Trk}} <$ 400 MeV

  where both M_{Trk} and M_{Miss} are computed from energy and momentum conservation.[1]

All momenta are evaluated at the point of closest approach (PCA) of each track, obtained by extrapolating the track inwards to the beam interaction point.

To ensure a good data quality and homogeneity of the data sample in use, data runs with a luminosity smaller than 25 nb^{-1} were excluded from the analysis, as were runs from the short 2002 energy-scan period and runs with bad trigger conditions [9].

3.2 Event selection

After the preselection, events have to fulfill the following selection criteria:

- at least two trigger sectors in the calorimeter [10] must be fired by clusters associated to the charged tracks in the event

- the events have to pass the software L3 trigger implemented in 2002 data taking to preserve events rejected by the trigger veto for cosmic ray events

- they have to pass an offline reconstruction filter, which removes machine background events

- two oppositely charged tracks have to satisfy

  - $|z_{PCA}| <$ 7 cm
  - $\varrho_{FH} <$ 50 cm

  where FH represents the first hit of a wire in the drift chamber, and the cut in $|z_{PCA}|$ further reduces the length of the cylinder to be crossed by the tracks to 14 cm, see Sec. 3.1

- the two charged tracks should have $50^\circ < \theta_\pi < 130^\circ$

[1] Assuming the presence of an unobserved photon and that the tracks belong to particles of the same mass, M_{trk} is computed from energy and momentum conservation:

$$\left(\sqrt{s} - \sqrt{|\mathbf{p}_+|^2 + M_{\text{trk}}^2} - \sqrt{|\mathbf{p}_-|^2 + M_{\text{trk}}^2}\right)^2 - (\mathbf{p}_+ + \mathbf{p}_-)^2 = 0$$

where $\mathbf{p}_\pm$ is the measured momentum of the positive (negative) particle, and only one of the four solutions is physical. Assuming the process is $e^+e^- \to \pi^+\pi^- X$, M_{Miss} is the invariant mass of the X particle in the final state.

- only photons within a cone of $\theta_\gamma < 15°$ around the beamline, narrow cones in Fig. 1, left, are accepted. The photon is not detected, its direction is reconstructed from event kinematics: $\vec{p}_\gamma \simeq \vec{p}_{miss} \equiv -\vec{p}_{\pi\pi} = -(\vec{p}_{\pi^+} + \vec{p}_{\pi^-})$. This separation of tracks and photon selection regions in the analysis greatly reduces the contamination from the resonant process $e^+e^- \to \phi \to \pi^+\pi^-\pi^0$ in which the π^0 mimics the missing momentum of the photon(s) and from the final state radiation process $e^+e^- \to \pi^+\pi^-\gamma_{\mathrm{F}SR}$. Since ISR-photons are mostly collinear with the beam line, a high statistics for the ISR signal events remains. However, a highly energetic photon emitted at small angle forces the pions also to be at small angles (outside the selection cuts), resulting in a suppression of events with $M^2_{\pi\pi} < 0.35$ GeV^2, see Fig. 1, right

- to avoid spiralizing tracks in the drift chamber, tracks are required to have $|p_T| > 160$ MeV or $|p_z| > 90$ MeV. This also ensures that tracks reach the electromagnetic calorimeter in the KLOE magnetic field of 0.52 T

- a particle ID estimator (PID) based on a pseudo-likelihood function using time-of-flight and calorimeter information is used to suppress radiative Bhabhas [11]. At least one of the two tracks must be recognized as "pion" (`or` configuration of the PID)

- $\phi \to \pi^+\pi^-\pi^0$ events are rejected by the cut

  $$M_{\mathrm{Trk}} = -\sqrt{1 - \left(\frac{M^2_{\pi\pi}}{0.85}\right)^2} \times 105. + 250. \tag{3.1}$$

  with $\mathrm{M}_{\mathrm{T}rk}$ in MeV and $M^2_{\pi\pi}$ in GeV^2, see Fig. 2, left. Above 0.815 GeV^2, a cut on $M_{\mathrm{T}rk} < 220$ MeV is applied.

- Signal events with pions are separated from muons by a cut $M_{\mathrm{T}rk} > 130$ MeV

Fig. 2, right, shows the spectrum for pions events after the selection.

4 The analysis

To obtain the cross section for $0° < \theta_\pi < 180°$ and $\theta_{\pi\pi} < 15°$, $\theta_{\pi\pi} > 165°$ we subtract the residual background from this spectrum and divide by the selection efficiency, acceptance, and integrated luminosity:

$$\frac{d\sigma_{\pi\pi\gamma}}{dM^2_{\pi\pi}} = \frac{\Delta N_{\mathrm{Obs}} - \Delta N_{\mathrm{Bkg}}}{\Delta M^2_{\pi\pi}} \frac{1}{\varepsilon_{\mathrm{Sel}}\varepsilon_{\mathrm{Acc}}} \frac{1}{\int \mathcal{L}dt}. \tag{4.1}$$

Fig. 4 shows the analysis flow. Apart from the offline filter (FILFO) correction and the L3 trigger efficiency, the selection efficiencies are evaluated via a *global* Monte Carlo efficiency, to which the corrections $\frac{\varepsilon^{Data}}{\varepsilon^{MC}}$ for the individual efficiencies (tracking, trigger) are applied. The global Monte Carlo efficiency (including the acceptance cut of $50^o < \theta_\pi < 130^o$) is shown in Fig. 3.

The background subtraction, the evaluation of the selection efficiency and the acceptance, the measurement of the integrated luminosity, and the unfolding of the experimental resolution on $M^2_{\pi\pi}$ (omitted from eq. (4.1) for clarity) are discussed below.

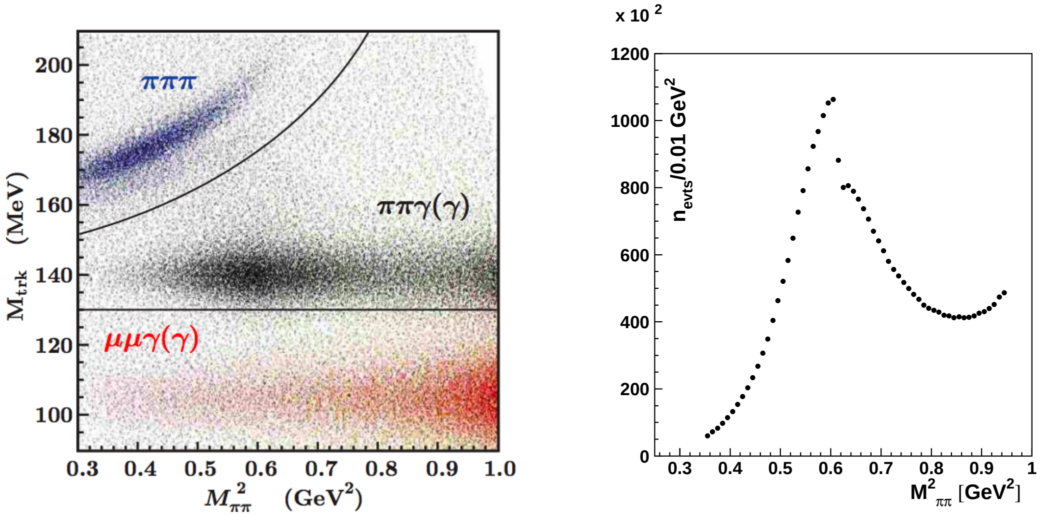

Figure 2: Left: Signal and background distributions in the $M_{\mathrm{T}rk} - M^2_{\pi\pi}$-plane . Right: Event spectra for pions after selection.

4.1 L3 (third level trigger) efficiency

The L3 efficiency (third level trigger) has been evaluated from an unbiased downscaled sample which retains a fraction of events independent of the L3 decision. Fig. 5 shows the L3 efficiency for 2002 data, which has to be compared with the cosmic ray veto efficiency in the published analysis which reached an inefficiency of 30% at high values of $M^2_{\pi\pi}$. Given the smallness of the L3 effect, it is considered to be negligible in the analysis, and a contribution of 0.1% is added to the overall systematic uncertainty in Table 9.

4.2 FILFO (offline background filter) efficiency

This filter, whose purpose is to identify background events before they enter the CPU-consuming pattern recognition and track fitting algorithms, contributed the largest experimental systematic error to the previous measurement [12]. A reworking of the offline background filter for the 2002 data allows to bring the systematic uncertainty on its efficiency to negligible level, while also increasing the efficiency itself. This was achieved by retaining an unbiased control sample during the data taking and the deactivation of the BHABREJ subfilter [13]. Fig. 6 shows the efficiency obtained in this way.

4.3 Estimation of background contributions

The relative contribution from the three main background channels

- $e^+e^- \to \mu^+\mu^-\gamma(\gamma)$
- $e^+e^- \to \pi^+\pi^-\pi^0$
- $e^+e^- \to e^+e^-\gamma(\gamma)$

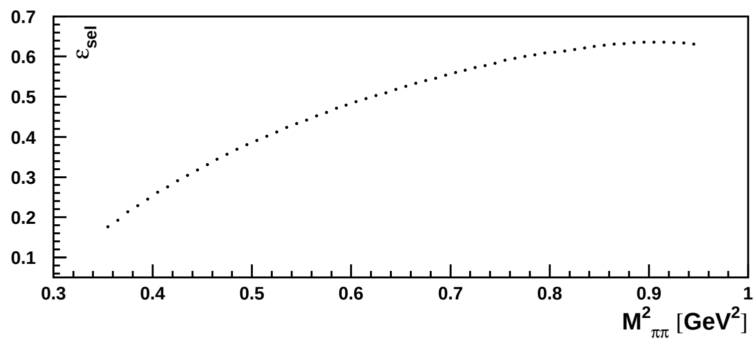

Figure 3: Global efficiency of the $\pi\pi\gamma$ event selection from Monte Carlo.

is estimated by fitting the sum of Monte Carlo distributions in M_{trk} for signal ($e^+e^- \to \pi^+\pi^-\gamma(\gamma)$) and the three background channels to the data distribution, using as free normalization parameters in the fit the weights w which allow to scale the Monte Carlo distributions for each channel. The fit is performed for 33 bin slices with a width of 0.02 GeV^2 in $M^2_{\pi\pi}$ between 0.32 and 0.98 GeV^2, using the M_{trk} distributions in each slice of $M^2_{\pi\pi}$. The fit procedure essentially follows the one described in [14], using the HBOOK [15] routine `HMCMLL` with small modifications according to [16, 17].

The main difference with [14] (apart from the larger number of $M^2_{\pi\pi}$ slices) is that all three background processes are treated simultaneously in the same fitting procedure. This was made possible by the much higher Monte Carlo statistics available (especially for the $\pi\pi\pi$ process) and the possibility to enlarge the fitting range to include also the full peak of the $\pi^+\pi^-\gamma$ events in the M_{trk} variable up to 180 - 220 MeV. The following Monte Carlo samples were used in the fitting procedure:

- 1500 pb^{-1} of $\pi^+\pi^-\gamma(\gamma)$ events, with both ISR and FSR at NLO
- 1500 pb^{-1} of $\mu^+\mu^-\gamma(\gamma)$ events, with both ISR and FSR at NLO
- 250 pb^{-1} of $\pi^+\pi^-\pi^0$ events
- 490 pb^{-1} of $e^+e^-\gamma$ events

For use in the fit, Monte Carlo distributions are adjusted using the corrections described in appendix B to procure better agreement with data. The fit is performed after the data has been corrected for the FILFO efficiency, the FILFO filter is thus not enforced for Monte Carlo events. The same holds for the L3 filter (see Sec. 4.1). To increase the sensitivity, the fit is performed without the cut of $M_{\text{trk}} > 130$ MeV shown in Fig. 2, left. This allows to include also the full peak of $\mu\mu\gamma$ events around 110 MeV.

As the contribution from $e^+e^-\gamma$ is very small, the fit is not sensitive enough to allow for a free normalization parameter for Bhabha events. Instead, the contribution of Bhabha events taken directly from Monte Carlo, using the integrated Monte Carlo luminosity as the normalization, and the Bhabha normalization parameter is fixed to 1. in the fit, as

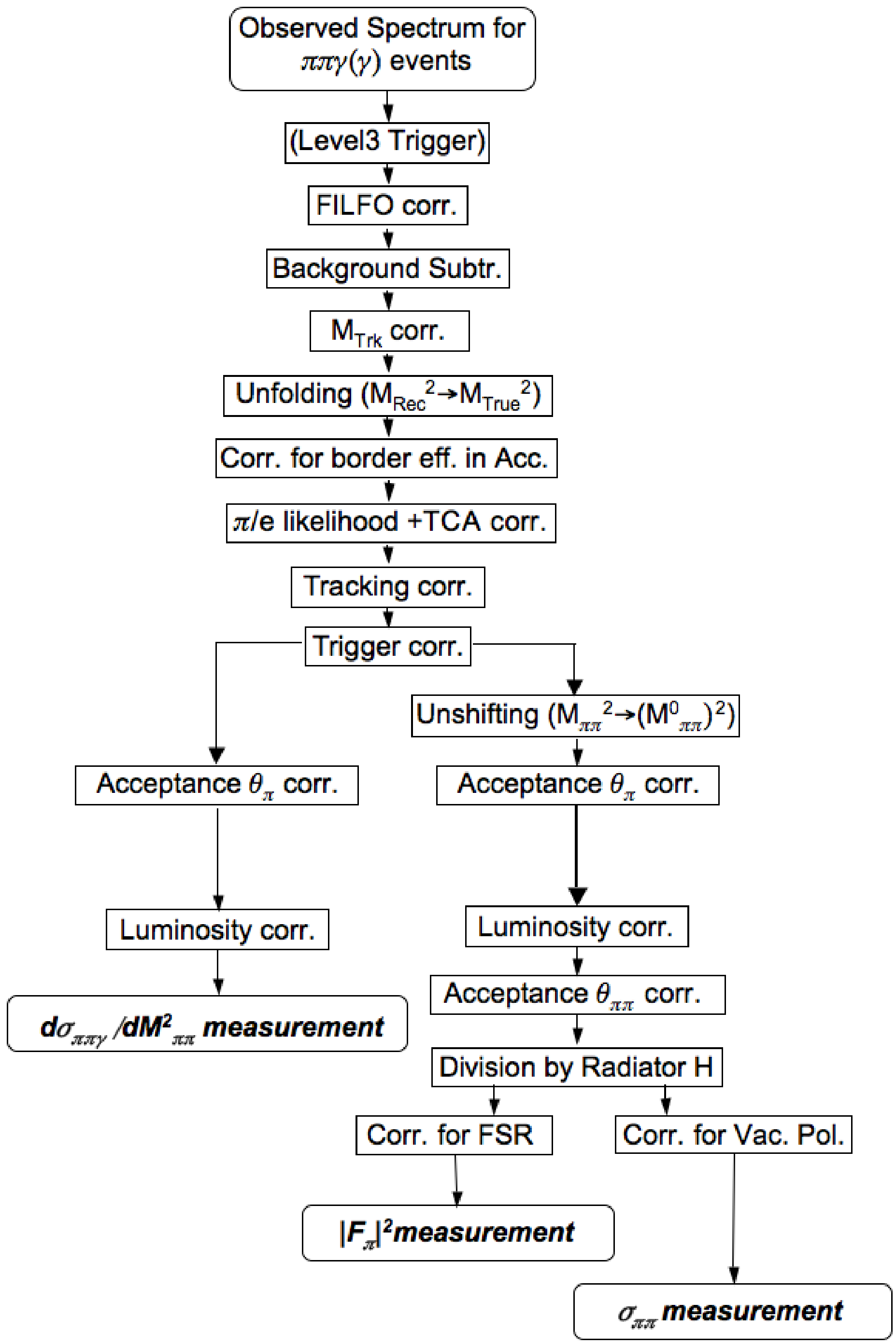

Figure 4: The description of the analysis flow.

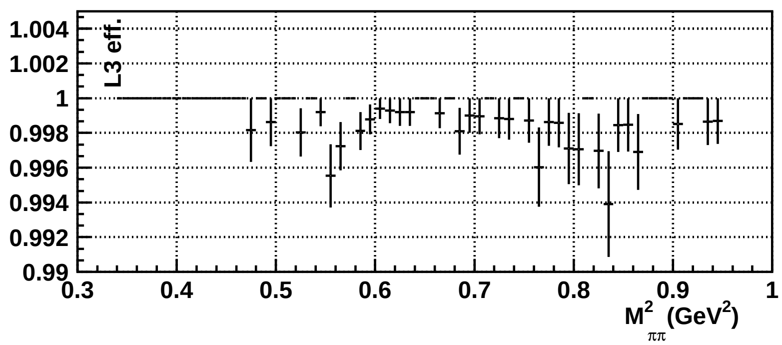

Figure 5: Efficiency of the L3 software trigger for pions.

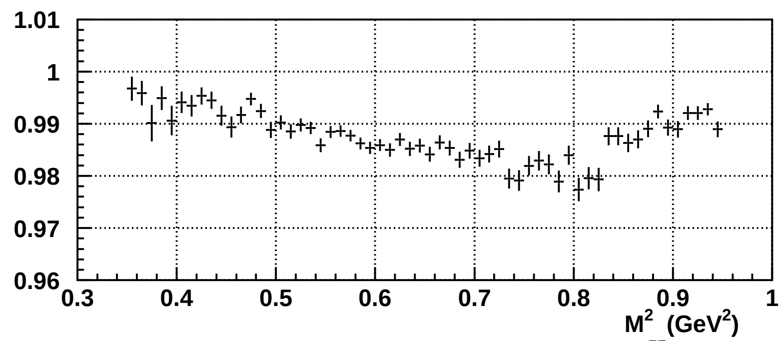

Figure 6: Efficiency of the FILFO reconstruction filter for pions.

is the contribution from $\pi\pi\pi$ between $0.6 < M_{\pi\pi}^2 < 0.7$ GeV^2. A cross check on the $ee\gamma$ Monte Carlo normalization is presented in a later section of this document (see Sec. 4.3.2). Some technical details on the fitting procedure in different ranges of $M_{\pi\pi}^2$:

- 0.32 - 0.60 GeV^2: Binwidth of 1.0 MeV in $M_{\rm trk}$, 4 Monte Carlo sources fitted to data, $ee\gamma$ normalization parameter fixed to 1.
- 0.60 - 0.70 GeV^2: Binwidth of 0.5 MeV in $M_{\rm trk}$, 4 Monte Carlo sources fitted to data, $ee\gamma$ and $\pi^+\pi^-\pi^0$normalization parameters fixed to 1.
- 0.70 - 0.98 GeV^2: Binwidth of 0.5 MeV in $M_{\rm trk}$, 3 Monte Carlo sources fitted to data, $ee\gamma$ normalization parameter fixed to 1.

The $\pi^+\pi^-\pi^0$ contribution in $M_{\rm trk}$ vanishes above 0.70 GeV^2, therefore the fit is performed using only 3 sources above this value. The results of the background fit procedure for each slice in $M_{\pi\pi}^2$ can be found in the appendix A.

Once the normalization parameters w are obtained in each slice of $M_{\pi\pi}^2$, they are applied on an event-by-event basis as weights in the filling of the histograms running the standard selection *including the cut in* $M_{\rm trk} > 130$ MeV with a binwidth in $M_{\pi\pi}^2$ of 0.01 GeV^2 (which is half the value used for the $M_{\pi\pi}^2$ slices used in the fit to obtain the Monte Carlo weights for each process, so each weight in a $M_{\pi\pi}^2$ slice is applied to two consecutive bins contained in this slice interval). From this the fraction of background events

$$f_{tot} \equiv N_{bkg}/N_{tot} = \frac{w_{\mu\mu\gamma} \cdot N_{\mu\mu\gamma}^{MC} + w_{\pi\pi\pi} \cdot N_{\pi\pi\pi}^{MC} + w_{ee\gamma} \cdot N_{ee\gamma}^{MC}}{N_{tot}} \tag{4.2}$$

is obtained in each bin of $M_{\pi\pi}^2$, relative to the number of data events $N_{\rm tot}$ found in this bin of $M_{\pi\pi}^2$. The data spectrum is then corrected in each bin of $M_{\pi\pi}^2$ with the factor $(1 - f_{\rm tot})$.

The statistical error on the combined background fraction in each bin i of $M_{\pi\pi}^2$ is calculated from

$$\begin{aligned}(\delta f_i)^2 = & \left(\frac{w_{\mu\mu\gamma,i} \cdot \delta N_{\mu\mu\gamma,i}}{N_{dat,i}}\right)^2 + \left(\frac{w_{\mu\mu\gamma,i} \cdot N_{\mu\mu\gamma,i} \cdot \delta N_{dat,i}}{N_{dat,i}^2}\right)^2 + \\ & \left(\frac{w_{\pi\pi\pi,i} \cdot \delta N_{\pi\pi\pi,i}}{N_{dat,i}}\right)^2 + \left(\frac{w_{\pi\pi\pi,i} \cdot N_{\pi\pi\pi,i} \cdot \delta N_{dat,i}}{N_{dat,i}^2}\right)^2 + \\ & \left(\frac{w_{ee\gamma,i} \cdot \delta N_{ee\gamma,i}}{N_{dat,i}}\right)^2 + \left(\frac{w_{ee\gamma,i} \cdot N_{ee\gamma,i} \cdot \delta N_{dat,i}}{N_{dat,i}^2}\right)^2\end{aligned} \tag{4.3}$$

where the w_i take into account the different amounts of integrated luminosity for data and Monte Carlo events. The errors on the w_i enter in the determination of the systematic uncertainty, which is described later in Sec. 4.3.4.

Table 4.3 and Figs. 7 and 8 show the result of the background evaluation.

4.3.1 Effect of the corrections for $M_{\rm trk}$ distributions in Monte Carlo

The Monte Carlo distributions in $M_{\rm trk}$ need to be adjusted to match the data distributions [18] (see appendix B.1). As can be seen from Table 4.3 and Fig. 9, the χ^2 of the

$\Delta M^2_{\pi\pi}$ (GeV^2)	$f_{\mu\mu\gamma(\gamma)}$ (%)	$w_{\mu\mu\gamma(\gamma)}$	$f_{\pi\pi\pi}$ (%)	$w_{\pi\pi\pi}$	$f_{ee\gamma(\gamma)}$ (%)	$w_{ee\gamma(\gamma)}$	χ^2_{min}/ndf	$P_{\chi^2>\chi^2_{min}}$ (%)
0.32-0.33	2.98±0.14	1.11±0.03	4.17±0.37	1.01±0.04	0.37±0.07	1±0	27.0/59	100.0
0.33-0.34	2.73±0.12		4.50±0.34		0.20±0.05			
0.34-0.35	2.33±0.10	1.06±0.02	3.90±0.27	0.89±0.03	0.27±0.05	1±0	35.6/66	99.9
0.35-0.36	2.58±0.09		3.89±0.24		0.16±0.04			
0.36-0.37	2.15±0.08	1.06±0.02	3.70±0.23	1.04±0.04	0.28±0.04	1±0	67.3/71	60.4
0.37-0.38	1.97±0.07		3.45±0.21		0.25±0.04			
0.38-0.39	1.75±0.06	1.07±0.02	3.09±0.18	1.07±0.04	0.19±0.03	1±0	61.8/67	65.7
0.39-0.40	1.72±0.05		2.80±0.16		0.21±0.03			
0.40-0.41	1.53±0.05	1.05±0.02	2.58±0.15	1.12±0.05	0.18±0.03	1±0	85.4/73	15.2
0.41-0.42	1.40±0.04		2.50±0.14		0.17±0.02			
0.42-0.43	1.31±0.04	1.06±0.02	2.26±0.12	1.18±0.05	0.18±0.02	1±0	55.8/74	94.4
0.43-0.44	1.21±0.03		2.08±0.11		0.17±0.02			
0.44-0.45	1.16±0.03	1.06±0.02	1.76±0.10	1.22±0.07	0.16±0.02	1±0	45.0/65	97.2
0.45-0.46	1.02±0.03		1.75±0.09		0.17±0.02			
0.46-0.47	0.91±0.02	1.02±0.02	1.73±0.08	1.25±0.06	0.15±0.02	1±0	66.1/77	80.7
0.47-0.48	0.88±0.02		1.37±0.07		0.13±0.01			
0.48-0.49	0.81±0.02	1.05±0.02	1.28±0.06	1.22±0.06	0.12±0.01	1±0	109.0/79	1.4
0.49-0.50	0.71±0.02		1.05±0.05		0.12±0.01			
0.50-0.51	0.71±0.02	1.07±0.02	0.97±0.05	1.17±0.07	0.11±0.01	1±0	101.0/80	5.7
0.51-0.52	0.65±0.01		0.87±0.04		0.11±0.01			
0.52-0.53	0.61±0.01	1.07±0.02	0.96±0.05	1.72±0.13	0.08±0.01	1±0	93.5/80	14.4
0.53-0.54	0.57±0.01		0.94±0.05		0.07±0.01			
0.54-0.55	0.54±0.01	1.07±0.01	0.83±0.04	1.82±0.18	0.08±0.01	1±0	80.3/81	50.1
0.55-0.56	0.53±0.01		0.74±0.04		0.08±0.01			
0.56-0.57	0.53±0.01	1.06±0.01	0.68±0.04	1.88±0.22	0.07±0.01	1±0	72.6/83	78.5
0.57-0.58	0.53±0.01		0.56±0.03		0.08±0.01			
0.58-0.59	0.55±0.01	1.08±0.01	0.64±0.04	2.44±0.29	0.08±0.01	1±0	97.8/86	18.0
0.59-0.60	0.54±0.01		0.52±0.03		0.09±0.01			
0.60-0.61	0.56±0.01	1.09±0.01	0.18±0.01	1.00±0.00	0.08±0.01	1±0	157.8/180	88.3
0.61-0.62	0.72±0.01		0.24±0.02		0.10±0.01			
0.62-0.63	0.84±0.01	1.09±0.01	0.19±0.01	1.00±0.00	0.13±0.01	1±0	117.5/184	100.0
0.63-0.64	0.86±0.01		0.14±0.01		0.13±0.01			
0.64-0.65	0.90±0.01	1.06±0.01	0.13±0.01	1.00±0.00	0.14±0.01	1±0	170.9/202	94.5
0.65-0.66	1.00±0.01		0.12±0.01		0.17±0.01			
0.66-0.67	1.06±0.02	1.07±0.01	0.09±0.01	1.00±0.00	0.16±0.01	1±0	146.4/210	100.0
0.67-0.68	1.16±0.02		0.09±0.01		0.18±0.01			
0.68-0.69	1.27±0.02	1.05±0.01	0.07±0.01	1.00±0.00	0.21±0.01	1±0	211.6/216	57.2
0.69-0.70	1.40±0.02		0.05±0.01		0.21±0.01			
0.70-0.71	1.51±0.02	1.05±0.01	0±0	1.00±0.00	0.19±0.01	1±0	200.2/218	80.1
0.71-0.72	1.68±0.02		0±0		0.23±0.01			
0.72-0.73	1.83±0.03	1.06±0.01	0±0	1.00±0.00	0.24±0.01	1±0	181.3/232	99.4
0.73-0.74	2.02±0.03		0±0		0.29±0.02			
0.74-0.75	2.10±0.03	1.05±0.01	0±0	1.00±0.00	0.31±0.02	1±0	228.8/236	61.9
0.75-0.76	2.33±0.03		0±0		0.32±0.02			
0.76-0.77	2.50±0.03	1.04±0.01	0±0	1.00±0.00	0.38±0.02	1±0	249.4/250	49.8
0.77-0.78	2.73±0.03		0±0		0.35±0.02			
0.78-0.79	2.94±0.04	1.03±0.01	0±0	1.00±0.00	0.41±0.02	1±0	202.1/254	99.3
0.79-0.80	3.18±0.04		0±0		0.43±0.02			
0.80-0.81	3.35±0.04	1.04±0.01	0±0	1.00±0.00	0.47±0.02	1±0	192.5/258	99.9
0.81-0.82	3.60±0.04		0±0		0.47±0.02			
0.82-0.83	3.79±0.04	1.03±0.01	0±0	1.00±0.00	0.51±0.02	1±0	187.6/210	86.5
0.83-0.84	3.99±0.04		0±0		0.47±0.02			
0.84-0.85	4.13±0.05	1.03±0.01	0±0	1.00±0.00	0.54±0.03	1±0	178.7/258	100.0
0.85-0.86	4.26±0.05		0±0		0.50±0.02			
0.86-0.87	4.44±0.05	1.01±0.01	0±0	1.00±0.00	0.52±0.03	1±0	163.0/190	92.2
0.87-0.88	4.69±0.05		0±0		0.53±0.03			
0.88-0.89	4.83±0.05	1.02±0.01	0±0	1.00±0.00	0.55±0.03	1±0	173.3/218	98.9
0.89-0.90	4.86±0.05		0±0		0.52±0.03			
0.90-0.91	4.85±0.05	1.00±0.01	0±0	1.00±0.00	0.50±0.02	1±0	193.8/218	87.9
0.91-0.92	4.86±0.05		0±0		0.48±0.02			
0.92-0.93	5.00±0.05	1.02±0.01	0±0	1.00±0.00	0.48±0.02	1±0	181.6/210	92.3
0.93-0.94	4.74±0.05		0±0		0.46±0.02			
0.94-0.95	4.64±0.04	1.01±0.01	0±0	1.00±0.00	0.38±0.02	1±0	209.8/192	18.0
0.95-0.96	4.46±0.04		0±0		0.37±0.02			
0.96-0.97	4.23±0.04	1.02±0.01	0±0	1.00±0.00	0.36±0.02	1±0	179.8/178	44.8
0.97-0.98	3.87±0.04		0±0		0.26±0.01			

Table 1: Results of the background fit.

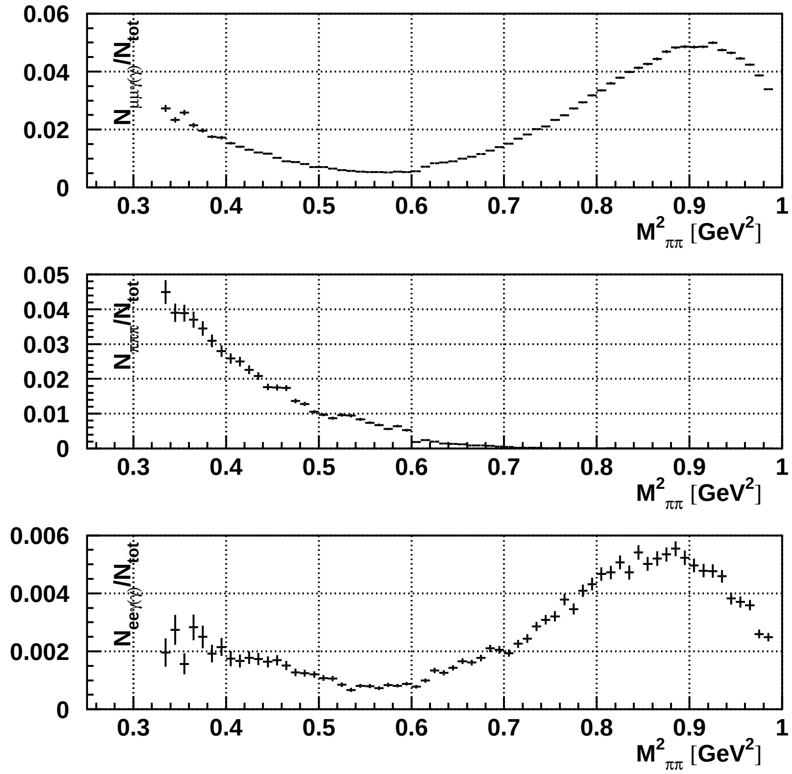

Figure 7: Fractional contributions for each of the three background channels to the total number of events present in the sample. Top: relative contribution of $\mu^+\mu^-\gamma(\gamma)$ events. Middle: relative contribution of $\pi^+\pi^-\pi^0$ events. Bottom: relative contribution of $e^+e^-\gamma(\gamma)$ events.

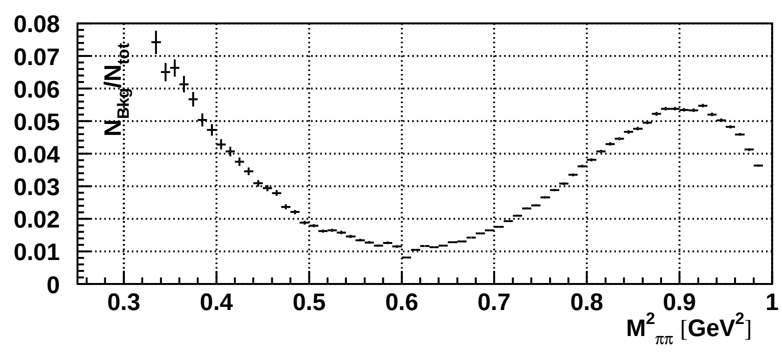

Figure 8: Sum of the 3 fractional background contributions shown in Fig. 7.

fit with this corrections is very good, except for some regions at small $M_{\pi\pi}^2$. The fit was also carried out using the corrections described in appendix B.2, which produce a good χ^2 below and above the ρ peak (but are much worse in the ρ mass region). Given the better χ^2 of this second corrections below 0.5 GeV^2, we use in this region the result of the background fit obtained from correcting the distributions with this second approach.

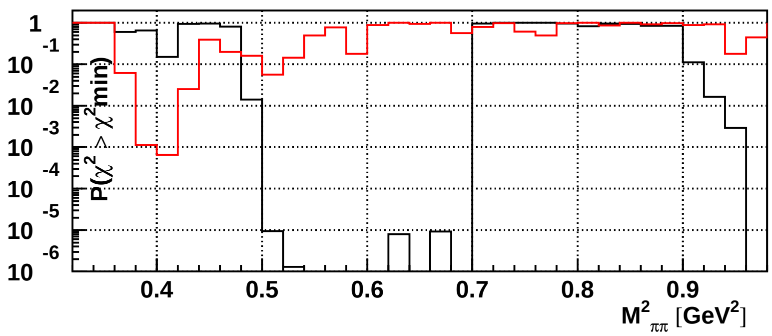

Figure 9: Probability for $\chi^2 > \chi^2_{min}$ for two different ways to correct $M_{\rm trk}$ distributions in Monte Carlo. Black: Using the corrections described in appendix B.1. Red: Using corrections described in appendix B.2. The second approach works better for $M_{\pi\pi}^2 < 0.5$ GeV^2, and has therefore been used in the background fitting for this region.

4.3.2 Cross check on normalization of $e^+e^-\gamma(\gamma)$ events

Since the background fit is not sensitive to the rather small contribution from Bhabha events to the signal events (see Fig. 7, lower plot), a cross check has been performed in the region between 0.7 and 0.9 GeV^2 to verify that the amount of Bhabha events in Monte Carlo has been produced with the correct normalization.

Data has been selected in bin slices of $M_{\pi\pi}^2$ using the `xor` condition for the π/e estimator (see Sec. 4.7). In this condition, events are selected only if one of the two tracks is identified to be a pion and the other one to be an electron. This greatly enhances the amount of Bhabha events with respect to $\pi\pi\gamma$ events. The absolute amount of Bhabha events does change very little when using the `xor` over the `or` selection used in the standard selection. This is different for the $\pi\pi\gamma$ events, of which only 3 - 4% of the events from the standard selection end up fulfilling the `xor` condition. In this way, while the absolute number of Bhabha events does not change between the two different selection schemes, they experience a relative enhancement respect to the $\pi\pi\gamma$ events. As of the already small amount of $\mu\mu\gamma$ events selected in the `or` condition (see Fig. 7, upper plot) again only 3 - 4% survive in the `xor` condition (the π/e separator treats muons and pions almost identically), in the absence of $\pi\pi\pi$ events, one can fit the distributions in $M_{\rm trk}$ with the simple sum of a polynomial (Bhabha) background and a Gaussian ($\pi\pi\gamma$) signal. Integrating the polynomial function obtained from the fit allows to estimate the Bhabha content in the $M_{\rm trk}$ distribution for each slice of $M_{\pi\pi}^2$ between 0.7 and 0.9 GeV^2 (where

$\pi\pi\pi$ events are absent, as their spectrum dies out above 0.7 GeV^2). Upscaling the integral of the Gaussian function obtained in the fit with the number $c = \frac{N^{or.}_{\pi\pi\gamma}}{N^{xor.}_{\pi\pi\gamma}}$, one recreates the number of $\pi\pi\gamma$ events in the `or` condition. From this, one can easily determine the amount of Bhabha events expected to survive the standard selection cuts. Comparing the outcome with the direct result from the Bhabha Monte Carlo, one can make a statement about the goodness of the normalization of the Bhabha Monte Carlo.

Fig. 10 shows the result of the fit in 10 slices of $M^2_{\pi\pi}$ between 0.7 and 0.9 GeV^2. Fig. 11 depicts the estimate of Bhabha contribution to the data spectrum obtained with the method described above, together with the direct outcome of the Bhabha Monte Carlo used in the background fit (see also Fig. 7, lower plot). The agreement is very good, justifying the use of the Bhabha Monte Carlo in the background fitting procedure without a free normalization parameter.

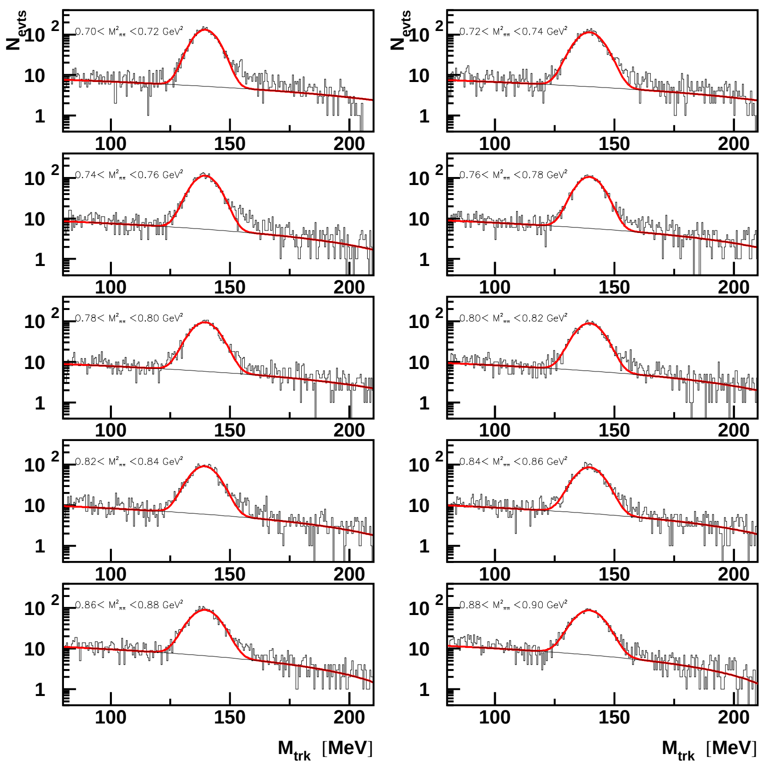

Figure 10: Result of the fit of the $M_{\rm trk}$ spectrum of data selected with the `xor` of the π/e estimator with a polynomial + Gaussian function. 10 slices of $M^2_{\pi\pi}$ between 0.70 and 0.90 GeV^2 are shown.

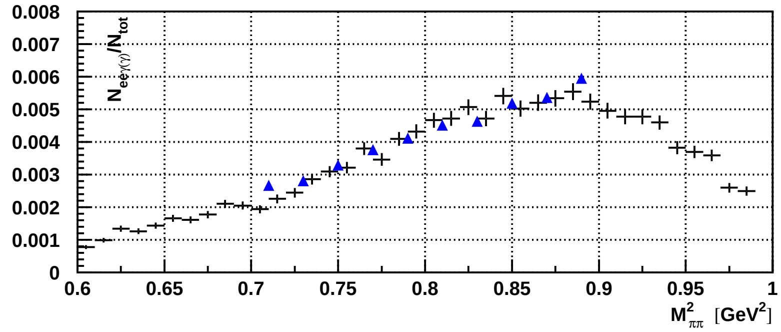

Figure 11: Result of the cross check on $ee\gamma$ normalization using `xor` selected data (blue triangles) and the outcome of the Monte Carlo (black crosses) used in the background fit.

4.3.3 Contributions from additional backgrounds

A potential contribution from events $e^+e^- \to e^+e^-\pi^+\pi^-$ has been evaluated using a sample of 800.000 reconstructed Monte Carlo events from the process $\phi \to \eta\gamma \to e^+e^-\pi^+\pi^-\gamma$, which have been provided by the KLOE $\eta \to e^+e^-\pi^+\pi^-$ analysis, and the EKHARA Monte Carlo generator [19, 20].

The EKHARA generator, which contains the diagrams shown in Fig. 12, was used to evaluate the effective cross section for having at least one pair of charged particles fulfilling the following requirements:

- $50^o < \theta_{\text{track}} < 130^o$
- $p_{T,\text{track}} > 160$ MeV or $p_{z,\text{track}} > 90$ MeV
- $150MeV < |\vec{p}_1| + |\vec{p}_2| < 1020MeV$
- $(-220)MeV < M_{\text{Miss}} < 120MeV$
- $130MeV < M_{\text{trk}} <$ elliptical cut in Fig. 2, left
- $\theta_\Sigma < 15^o$ or $\theta_\Sigma > 165^o$
- At least one of the tracks fulfilling these conditions should be identified as a pion

The last condition is imposed since 2 electrons passing all conditions would be rejected by the π/e likelihood estimator.

To accommodate the reconstruction efficiency into the EKHARA effective cross section, the $\phi \to \eta\gamma \to e^+e^-\pi^+\pi^-\gamma$ Monte Carlo events (which were obtained from a Monte Carlo generator interfaced with the KLOE detector simulation) were used to find out how many tracks with $50^o < \theta_{\text{track}} < 130^o$ and $p_{T,\text{track}} > 160$ MeV or $p_{z,\text{track}} > 90$ MeV would fulfill the following conditions:

- each track must cross a cylinder centered around the beam interaction point with 14 cm length and 8 cm radius

- the transverse distance to the IP of the first (wire) hit in the drift chamber of each track must be smaller than 50 cm

It was found that for pions, this reconstruction efficiency from Monte Carlo is $\varepsilon_\pi = 0.94$, while for the electrons, one obtains $\varepsilon_e = 0.98$, both flat in θ and equal for both charges. Using these values in EKHARA as a weight for the charged tracks surviving the requirements mentioned above, one obtains a total cross section of $\sigma_{ee\pi\pi} = (46.98 \pm 0.15)$pb.

Fig. 13 shows the relative contribution from $e^+e^- \to e^+e^-\pi^+\pi^-$ events to the spectrum in Fig. 2, right. This plot was obtained by using the effective cross section obtained from EKHARA to estimate the effective yield of $e^+e^-\pi^+\pi^-$ events for 241.4pb^{-1} in bins of the invariant mass squared of the pair of tracks, assuming for both tracks to have the mass of a charged pion. This event yield was then compared to the data spectrum after selection.

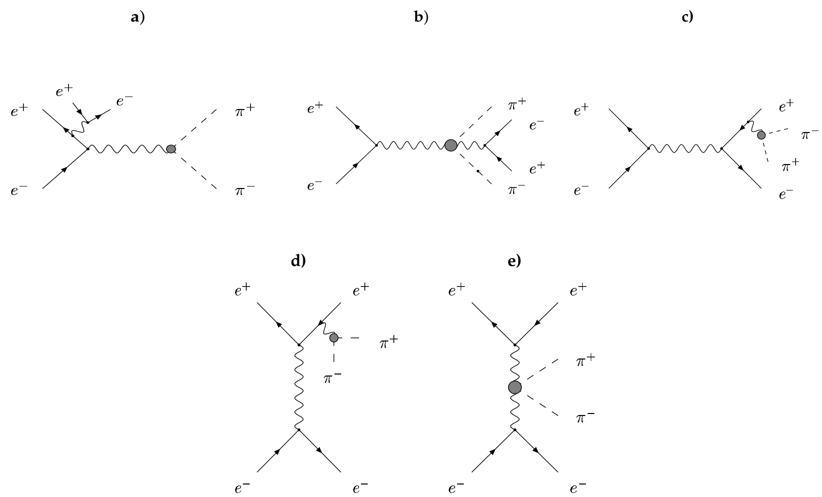

Figure 12: Diagrams contributing to the process $e^+e^- \to e^+e^-\pi^+\pi^-$ (figure taken from [20]).

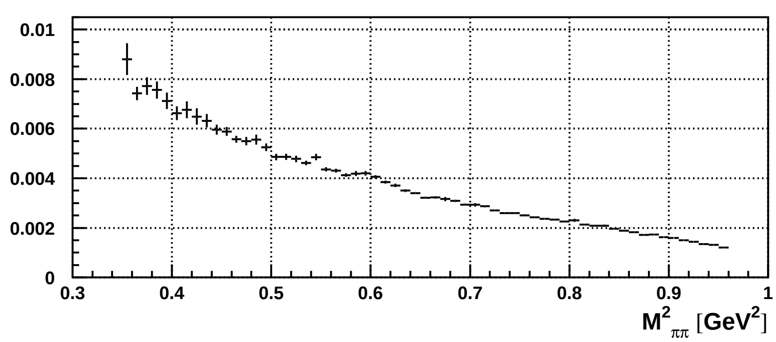

Figure 13: Relative contribution from the process $e^+e^- \to e^+e^-\pi^+\pi^-$ to the data spectrum.

To evaluate an eventual contribution from $e^+e^- \to e^+e^-\mu^+\mu^-$ (in which the muons are misidentified as pions), we have used the NEXTCALIBUR Monte Carlo generator [21]. Applying acceptance cuts and the cut on $M_{\rm trk}$ shown in Fig. 2, left, on the pair of muons produced in the final state, the obtained cross section gives an event yield which is compatible with zero in most of the range of $M^2_{\pi\pi}$, reaching a relative contribution to the data spectrum of 0.05% only below 0.5 GeV^2. This contribution is therefore considered negligible for our analysis.

The additional background contribution from $\phi \to (f_0 + \sigma)\gamma \to \pi^+\pi^-\gamma$ has been estimated with PHOKHARA6.1, where the Achasov model fitted to $\pi^0\pi^0\gamma$ was implemented [22]. This contribution has been found to be negligible within the small angle selection cuts described in Sec. 3.2.

The $e^+e^- \to \omega\gamma_{ISR} \to \pi^+\pi^-\pi^0\gamma$ contribution ($\sigma = 5$ nb) has been studied with PHOKHARA5.0 interfaced with GEANFI detector simulation for the KLOE experiment [23], 10^5 events were generated in the full phase space. No events survived to the $\pi^+\pi^-\gamma$ selection cuts, mostly due to the cut on missing mass in the preselection rejecting events with $m_{\rm Miss} > 120$ MeV, which is the case for $\omega \to \pi^+\pi^-\pi^0$ events.

4.3.4 Evaluation of the systematic uncertainty

The systematic uncertainty due to the background estimation has two parts:

- The contribution from the error on the weights w obtained in the fit procedure
- The contribution from $e^+e^- \to e^+e^-\pi^+\pi^-$ events (see Sec. 4.3.3)

The errors on the weights w obtained in the fit are enlarged if $P_{\chi^2>\chi^2_{min}}$ is smaller than 5% according to

$$\delta w \longrightarrow \sqrt{\frac{\chi^2_{min}}{\rm ndf}} \cdot \delta w \tag{4.4}$$

Since $\delta\sigma_{\pi\pi\gamma}$ is proportional to $(1-f) = 1 - f_{\mu\mu\gamma} - f_{\pi\pi\pi} - f_{ee\gamma}$, the relative uncertainty on the cross section from the weights is given by[2]:

$$\frac{\delta\sigma_{\pi\pi\gamma}}{\sigma_{\pi\pi\gamma}} = \frac{\sqrt{\left(\frac{\delta w_{\mu\mu\gamma}}{w_{\mu\mu\gamma}} f_{\mu\mu\gamma}\right)^2 + \left(\frac{\delta w_{\pi\pi\pi}}{w_{\pi\pi\pi}} f_{\pi\pi\pi}\right)^2 + 2\cdot\varrho_{\mu\mu\gamma,\pi\pi\pi}\frac{\delta w_{\mu\mu\gamma}}{w_{\mu\mu\gamma}} f_{\mu\mu\gamma}\frac{\delta w_{\pi\pi\pi}}{w_{\pi\pi\pi}} f_{\pi\pi\pi} + \left(\frac{\delta w_{ee\gamma}}{w_{ee\gamma}} f_{ee\gamma}\right)^2}}{1 - f_{\mu\mu\gamma} - f_{\pi\pi\pi} - f_{ee\gamma}} \tag{4.5}$$

The parameter $\varrho_{\mu\mu\gamma,\pi\pi\pi}$ describes the correlation between the fit parameters $w_{\mu\mu\gamma}$ and $w_{\pi\pi\pi}$. Its value lies between -0.1 and +0.1. The contribution from eq. 4.5 to the relative uncertainty on the $\sigma_{\pi\pi\gamma}$ cross section is smaller than 0.05% above 0.6 GeV^2, and between 0.08 and 0.16% below (this reflects the fact that above 0.6 GeV^2, the contribution from $\pi\pi\pi$ events is not fitted with a free normalization parameter anymore).

For the events $e^+e^- \to e^+e^-\pi^+\pi^-$, the relative contribution as in Fig. 13 has been subtracted from the spectrum, and a conservative error of 50% (including a 25% error of the generator [24]) is taken as an uncertainty on the measurement.

[2] As the Bhabha events are not fitted, but merely included in the fit without a free normalization parameter, $w_{ee\gamma} = 1$ and $\delta w_{ee\gamma} = 0$, as seen in Table 4.3; therefore the Bhabhas do not contribute to the numerator in eq. 4.5.

$M^2_{\pi\pi}$ (GeV^2)	0.005	0.015	0.025	0.035	0.045	0.055	0.065	0.075	0.085	0.095
0.3						0.5	0.4	0.4	0.4	0.4
0.4	0.4	0.4	0.4	0.3	0.3	0.3	0.3	0.3	0.3	0.3
0.5	0.3	0.3	0.3	0.2	0.3	0.2	0.2	0.2	0.2	0.2
0.6	0.2	0.2	0.2	0.2	0.2	0.2	0.2	0.2	0.2	0.2
0.7	0.2	0.1	0.1	0.1	0.1	0.1	0.1	0.1	0.1	0.1
0.8	0.1	0.1	0.1	0.1	0.1	0.1	0.1	0.1	0.1	0.1
0.9	0.1	0.1	0.1	0.1	0.1					

Table 2: Systematic error in % due to background subtraction in 0.01 GeV^2 bin intervals of $M^2_{\pi\pi}$. The bin center is given by the sum of the values in the first row and first column.

Fig. 14 and Table 2 show the final systematic uncertainty on the measurement due to the effects from the background evaluation. This introduces an error of 0.3% on the value of $\Delta^{\pi\pi} a_\mu$.

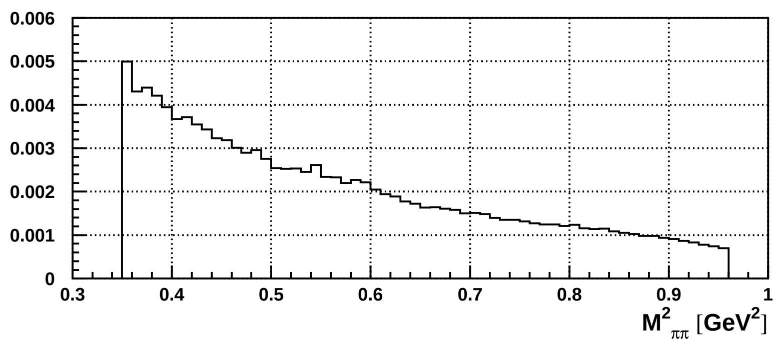

Figure 14: Systematic uncertainty to the cross section measurement due to background.

4.4 Efficiency estimation for the cuts in $M_{\rm trk}$

Once the background is subtracted from the spectrum, we correct for the efficiencies of the kinematical variables $M_{\rm trk}$. It is evaluated from the Monte Carlo production for $\pi^+\pi^-\gamma(\gamma)$events with the PHOKHARA generator. As this generator has been interfaced with the GEANFI, we can extract the efficiency as a function of $(M^2_{\pi\pi})^{rec}$. The kinematical efficiency is thus the part of the *Global Monte Carlo efficiency* which is evaluated in $(M^2_{\pi\pi})^{rec}$. From the outcome of the background fit procedure (see Sec. 4.3), one finds that the corrections performed to the Monte Carlo distributions in reconstructed observables result in a very good agreement in the shapes of the distributions (see e.g. χ^2/ndof values in Table 4.3 or the plots of fit results in appendix A). We therefore do not perform an additional correction concerning a difference between $M_{\rm trk}$ efficiencies obtained from data and from Monte Carlo.

The systematic uncertainty has been estimated by performing the analysis changing the cut $M_{\rm trk} = 130$ MeV which separates $\pi\pi\gamma$ from $\mu\mu\gamma$ events to $M_{\rm trk} = 120$ MeV. A fractional difference of 0.1% (flat in $M_{\pi\pi}$) on the $\pi\pi\gamma$ cross section is found. A similar change can be expected from a variation of the elliptical cut in the $M_{\rm trk}$-$M^2_{\pi\pi}$-plane (Fig. 2, left). A value of 0.2% is thus taken as systematic error due to the $M_{\rm trk}$ cut.

4.5 Correcting for the detector resolution

The correction for the detector resolution (often called *unfolding*) in $M^2_{\pi\pi}$ takes place right after the correction for the kinematical efficiencies (see Fig. 4). As this implies the passage from $(M^2_{\pi\pi})^{rec}$ to $(M^2_{\pi\pi})^{true}$, subsequent corrections have to be performed in $(M^2_{\pi\pi})^{true}$.

The number of events in bin i of $(M^2_{\pi\pi})^{true}$ can be related to the spectrum of observed events in bins j of $(M^2_{\pi\pi})^{rec}$ via

$$N_i^{true} = \sum_{j=1} P(N_i^{true}|N_j^{rec}) \cdot N_j^{rec} \tag{4.6}$$

where the sum runs over all bins of the reconstructed quantity $M^2_{\pi\pi}$. The problem then consists in finding the quantity $P(N_i^{true}|N_j^{rec})$, which describes the bin-to-bin migration of events due to the event reconstruction (and thus the detector resolution). This quantity determines the contribution of an observed event in bin j of $(M^2_{\pi\pi})^{rec}$ to the bin i in $(M^2_{\pi\pi})^{true}$.

We have used to methods to evaluate $P(N_i^{true}|N_j^{rec})$:

- Evaluating $P(N_i^{true}|N_j^{rec})$ directly from a sample of reconstructed $\pi^+\pi^-\gamma(\gamma)$ Monte Carlo events, using the normalization condition

$$\sum_{i=1}^{n_{true}} P(N_i^{true}|N_j^{rec}) = 1 \tag{4.7}$$

  This corresponds to the statement that each observed event must come from one or more bins of the *true* values of $M^2_{\pi\pi}$. Then the correction reduces to a simple *matrix multiplication* of $P(N_i^{true}|N_j^{rec})$ with the vector of the observed spectrum in bins of $(M^2_{\pi\pi})^{rec}$. However, a bias can be introduced due to the parametrization of $|F_\pi|^2$ used in the Monte Carlo generation.

- Evaluating $P(N_i^{true}|N_j^{rec})$ using Bayes' theorem [25]. This is a more sophisticated procedure, reducing the bias from the parametrization for $|F_\pi|^2$ used in the Monte Carlo production by defining $P(N_i^{true}|N_j^{rec})$ as

$$P(N_i^{true}|N_j^{rec}) = \frac{P(N_j^{rec}|N_i^{true}) \cdot P_0(N_i^{true})}{\sum_{l=1}^{n_{true}} P(N_j^{rec}|N_l^{true}) \cdot P_0 N_l^{true}} \tag{4.8}$$

  where the *initial probability* $P_0(N_l^{true})$ is changed in an iterative procedure to become more and more consistent with the distribution of the N_i^{true}. Both $P_0(N_l^{true})$ and the *response matrix* $P(N_j^{rec}|N_i^{true})$ are obtained from a Monte Carlo production of $\pi^+\pi^-\gamma(\gamma)$ events. An easily modifiable `FORTRAN` code from the authors' webpage [26] performs the necessary calculations and iterations.

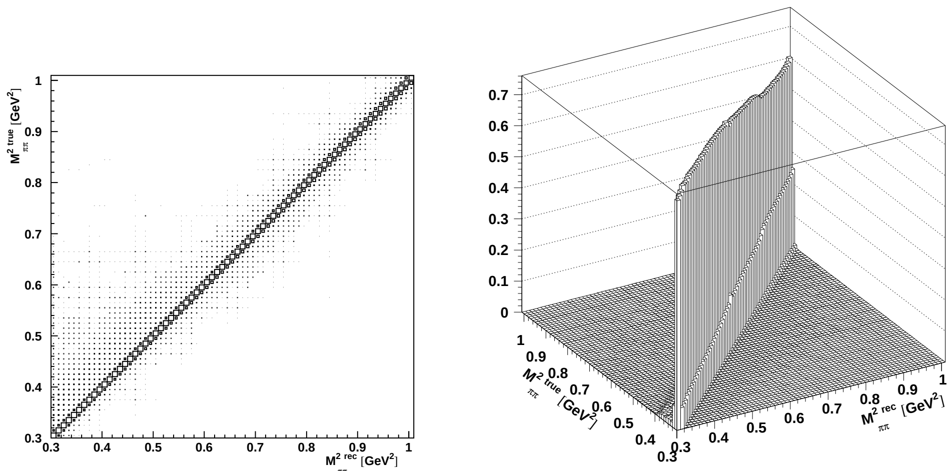

Figure 15: The probability matrix $P(N_i^{true}|N_j^{rec})$ (*smearing matrix*) which represents the correlation between generated (true) and reconstructed values for $M^2_{\pi\pi}$.

In Fig. 15, the probability matrix $P(N_i^{true}|N_j^{rec})$ from Monte Carlo is shown. The high precision of the KLOE drift chamber results in an almost diagonal matrix. Both methods give rather similar results. Following the advice from the author of the Bayesian unfolding method, we perform a smoothing of the spectrum to be unfolded to avoid fluctuations caused by statistical limitations. The smoothing is performed only in the regions below 0.5 GeV^2 and between 0.7 and 0.95 GV^2, and not in the region of the $\rho - \omega$ interference. Fig. 16 shows the outcome of the two methods, compared to the original input spectrum. In the analysis, we use the Bayesian approach, while the Matrix Multiplication method is used to estimate the systematic uncertainty. It has also been verified that the outcome of the procedure does not depend on the χ^2-like cutoff value used to terminate the iteration loop. Fig. 17 shows the covariance matrix obtained in the Bayesian unfolding method. It essentially maintains the diagonal structure of the smearing matrix without getting broader. As an estimate for the systematic uncertainty on the differential $d\sigma_{\pi\pi\gamma}/dM^2_{\pi\pi}$ cross section, the $\pi^+\pi^-$cross section and $|F_\pi|^2$, we take the absolute value of the difference between the two methods. As can be seen in Fig. 18, this gives a significant contribution only near the $\rho - \omega$ interference region, where the smallness of the width of the ω meson introduces strong variations in the shape of $|F_\pi|^2$ over small intervals of $M^2_{\pi\pi}$. Table 3 shows the values of the relative systematic uncertainty on our measurement in %, only non-negligible in the region between 0.58 and 0.63 GeV^2. Please note that the unfolding has a negligible effect on the integral on $a_\mu^{\pi\pi}$, as it simply moves events between adjacent bins. Therefore, the uncertainty given in Table 3 should not be taken into account when evaluating the integral on $a_\mu^{\pi\pi}$ from $\sigma_{\pi\pi}$.

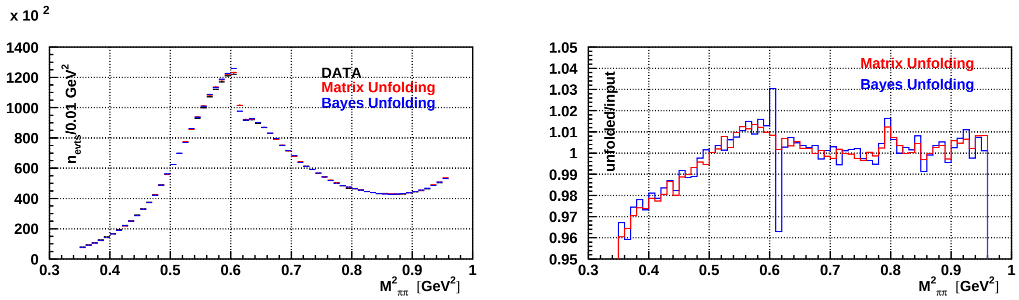

Figure 16: Left: Input spectrum (black) in bins of $(M^2_{\pi\pi})^{rec}$ and unfolded spectrum for matrix multiplication method (red) and Bayesian method (blue) in bins of $(M^2_{\pi\pi})^{true}$. Right: Ratio of the unfolded over the input spectrum, for the matrix multiplication method (red) and the Bayesian method (blue) in bins of $M_{\pi\pi}$.

$M^2_{\pi\pi}$ (GeV^2)	0.585	0.595	0.605	0.615	0.625
$\delta_{unf}(\%)$	0.4	0.3	2.1	4.0	0.4

Table 3: Systematic error in % on $d\sigma(e^+e^- \to \pi^+\pi^-\gamma)/dM^2_{\pi\pi}$, $\sigma(e^+e^- \to \pi^+\pi^-)$ and $|F_\pi|^2$ due to the correction for detector resolution in 0.01 GeV^2 intervals. The indicated values for $M^2_{\pi\pi}$ represent the center of the bin. Outside this interval the effect is negligible.

4.6 Tracking efficiency

The efficiency of reconstructing the pion track is measured per single charge, both on Monte Carlo and data samples, conditioned to the presence of a tagging track of opposite sign. More specifically, the efficiency to find the pion track of a given sign is parametrized as a function of momentum and polar angle slices of the candidate track.

We studied Monte Carlo events of $\pi^+\pi^-\gamma$ and two control samples from data: $\pi^+\pi^+\pi^0$ events, that are almost background free and provide large statistics (the cross section $\sigma_{e^+e^-\to\pi^+\pi^-\pi^0}$ is about 1 order of magnitude larger than the signal), but they are limited to probe track momentum $p < 400$ MeV; and $\pi^+\pi^-\gamma$ events, which are contaminated with $\pi^+\pi^+\pi^0$ and $\mu^+\mu^-\gamma$ events, such that hard cuts are applied and the resulting statistics is small, but it allows to cover larger momentum bins.

The selection of the $\pi^+\pi^-\pi^0$ data sample is based on the following requirements applied on a sample of 5 pb^{-1} of "raw" data:

(3π.1) at least one tagging track "good", namely first hit $\sqrt{x^2_{\rm FH} + y^2_{\rm FH}} < 50$ cm and point of the closest approach (pca) of the backward track extrapolation $\sqrt{x^2_{\rm PCA} + y^2_{\rm PCA}} < 8$ cm, $|z_{\rm PCA}| < 7$ cm;

(3π.2) the tagging track must have a cluster associated to it (after extrapolating the track to the calorimeter and looking for a cluster within a sphere of radius = 90 cm) recognized as a pion – PID function $\log \mathcal{L}_\pi/\mathcal{L}_e > 0$;

(3π.3) 2 and only 2 photons, namely prompt clusters – according to the standard prescrip-

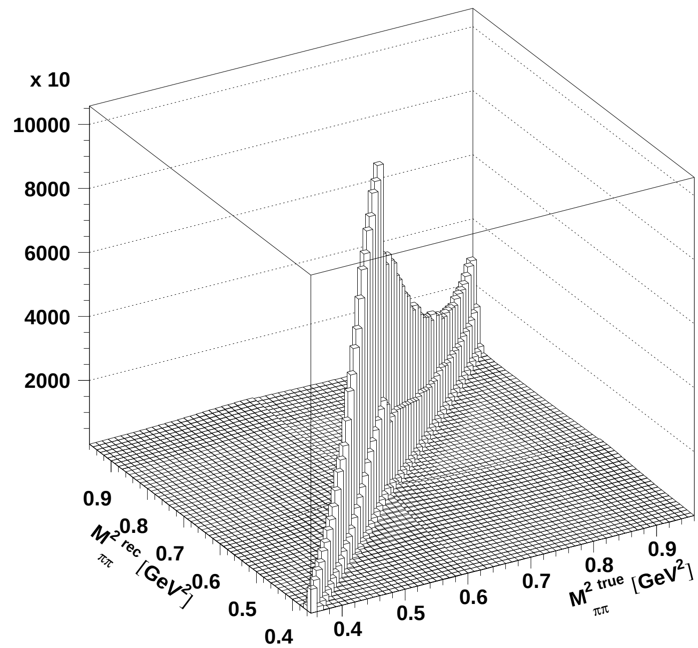

Figure 17: Covariance matrix obtained from the Bayesian unfolding method.

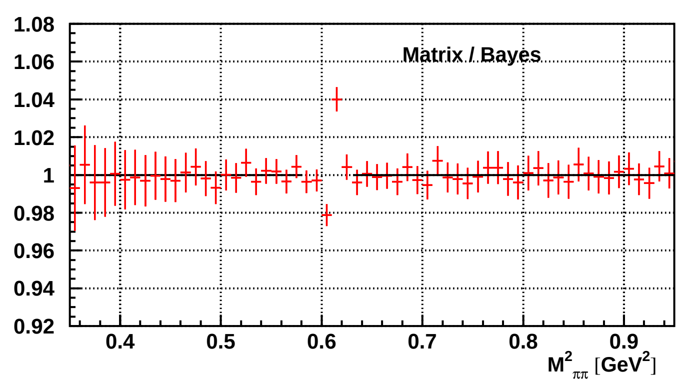

Figure 18: Estimate of the systematic uncertainty on the points of the differential $d\sigma_{\pi\pi\gamma}/dM^2_{\pi\pi}$ cross section, the $\pi^+\pi^-$cross section and $|F_\pi|^2$ due to the unfolding procedure. It has been obtained by dividing the unfolded spectrum from the Matrix Multiplication method for the unfolded spectrum from the Bayesian method. The fits outside the region of the $\rho - \omega$ interference give values compatible with 1.

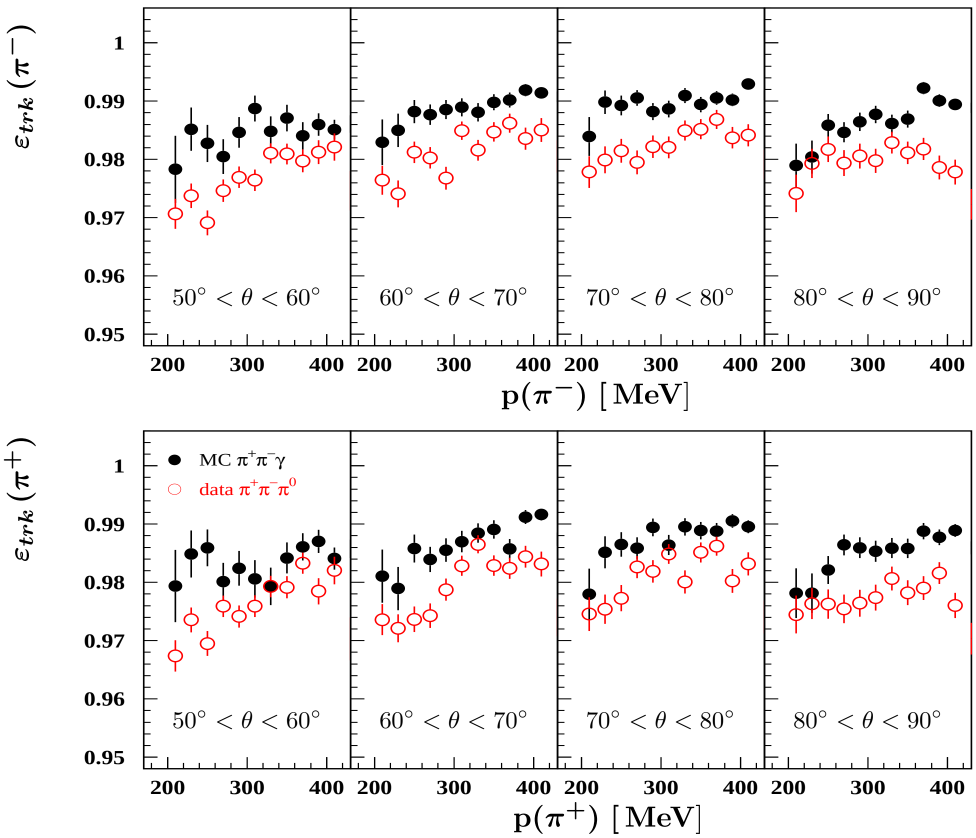

Figure 19: Data vs. Monte Carlo comparison of tracking efficiencies for negative (top) and positive (bottom) tracks, as a function of the expected momentum, for different polar angle range. Pions are obtained from a sample of $\pi^+\pi^-\pi^0$ data and $\pi^+\pi^-\gamma$ MC events.

tion $|t_{\rm clu} - r_{\rm clu}/c| < 5\sigma_t$ – and neutral, *i.e.* neither associated to the tagging track nor to other tracks;

(3π.4) the 2 photons must have energy > 50 MeV and be distant > 60 cm, each other.

Momenta of the two photon clusters are improved by means of a χ^2 minimization procedure, where measured variables and constraints are sketched in the following table:

10 measurements: 5 for each γ	4 constraints
$E_\gamma \equiv \gamma$ cluster energy	$M^2_{\gamma\gamma} = m^2_{\pi^0}$
$\vec{r}_\gamma \equiv \gamma$ cluster space coordinates	$M^2_{Miss}(\sum E_i, \lvert\sum \vec{p}_i\rvert) = m^2_{\pi^+}$
$t_\gamma \equiv \gamma$ cluster time	$t_\gamma - \lvert\vec{r}_\gamma\rvert/c = 0$, for each γ

where the missing mass, $M_{\rm Miss}$, is evaluated from momenta of the 2 photons and of the tagging track.

The following criteria to select $\pi^+\pi^-\gamma$ events from a sample of 90 pb^{-1} of "raw" data and 110 pb^{-1} of Monte Carlo – with scale factor 6, *i.e.* effective 660 pb^{-1} – are used:

($\pi\pi\gamma$.1) at least one tagging track "good", namely first hit $\sqrt{x^2_{\rm FH} + y^2_{\rm FH}} < 50$ cm and point of the closest approach (pca) of the backward track extrapolation $\sqrt{x^2_{\rm PCA} + y^2_{\rm PCA}} < 8$ cm, $|z_{\rm PCA}| < 7$ cm;

($\pi\pi\gamma$.2) the tagging track must have an associated cluster (after extrapolating the track to the calorimeter and looking for a cluster within a sphere of radius = 90 cm) recognized as a pion – PID function $\log \mathcal{L}_\pi/\mathcal{L}_e > 0$;

($\pi\pi\gamma$.3) 1 and only 1 photon with energy > 50 MeV;

($\pi\pi\gamma$.4) the tagging track must have momentum $|\vec{p}_{tag}| > 460$ MeV, to suppress $\pi^+\pi^-\pi^0$ events on data;

($\pi\pi\gamma$.5) the expected track must have mass $M_{\rm Miss} < 120$ MeV – evaluated using 4-momentum conservation on momenta of the photon and the tagging track – and `MLP` < 0.3, to suppress $\mu^+\mu^-\gamma$ events on data.

No difference is found on Monte Carlo with and without requirements ($\pi\pi\gamma$.4) and ($\pi\pi\gamma$.5).

For all three samples, the event is efficient if a fitted track with opposite charge with respect to the tagging track, and with $\sqrt{x^2_{\rm FH} + y^2_{\rm FH}} < 50$ cm, $\sqrt{x^2_{\rm PCA} + y^2_{\rm PCA}} < 8$ cm and $|z_{\rm PCA}| < 7$ cm – namely the same quality cuts on tracks used in the event selection – is found, for given values of expected momentum p, and polar angle θ.

Fig. 19 shows the comparison of the tracking efficiency between pions from $\pi^+\pi^-\pi^0$ data and from the signal Monte Carlo sample, as a function of the expected momentum, for different polar angle ranges. Fig. 20 shows the same comparison for pions of $\pi^+\pi^-\gamma$ data and Monte Carlo samples.

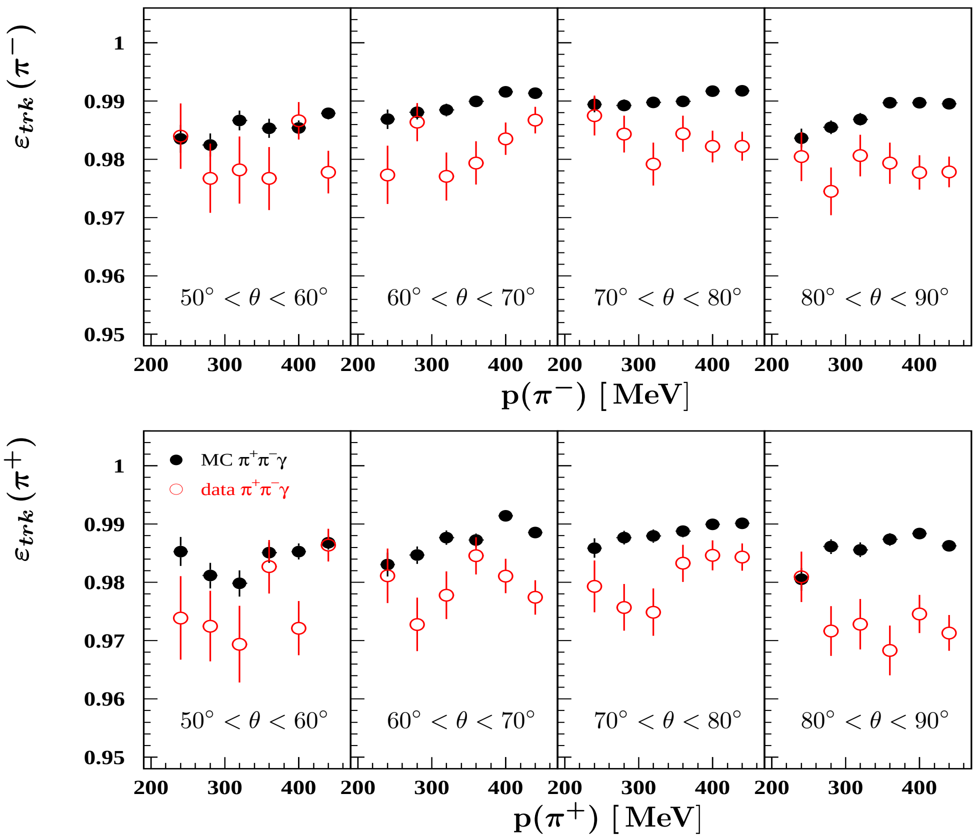

Figure 20: Data vs. Monte Carlo comparison of tracking efficiencies for negative (top) and positive (bottom) tracks, as a function of the expected momentum, for different polar angle range. Pions are obtained from a sample of $\pi^+\pi^-\gamma$ data and $\pi^+\pi^-\gamma$ MC events.

For each θ slice, we evaluated data over Monte Carlo corrections as the ratio of the tracking efficiencies as a function of p, for pions of both signs:

$$c_{3\pi}(\theta_{\pi^\pm}, p_{\pi^\pm}) = \frac{\varepsilon^{data}_{\pi^+\pi^-\pi^0}(\theta_{\pi^\pm}, p_{\pi^\pm})}{\varepsilon^{MC}_{\pi^+\pi^-\gamma}(\theta_{\pi^\pm}, p_{\pi^\pm})}, \qquad c_{\text{ppg}}(\theta_{\pi^\pm}, p_{\pi^\pm}) = \frac{\varepsilon^{data}_{\pi^+\pi^-\gamma}(\theta_{\pi^\pm}, p_{\pi^\pm})}{\varepsilon^{MC}_{\pi^+\pi^-\gamma}(\theta_{\pi^\pm}, p_{\pi^\pm})}$$

Both Fig. 21 and Fig. 22 show that corrections result almost flat for the momentum of interest, and in good agreement for pions of the same sign and same polar angle range, obtained from two different data samples.

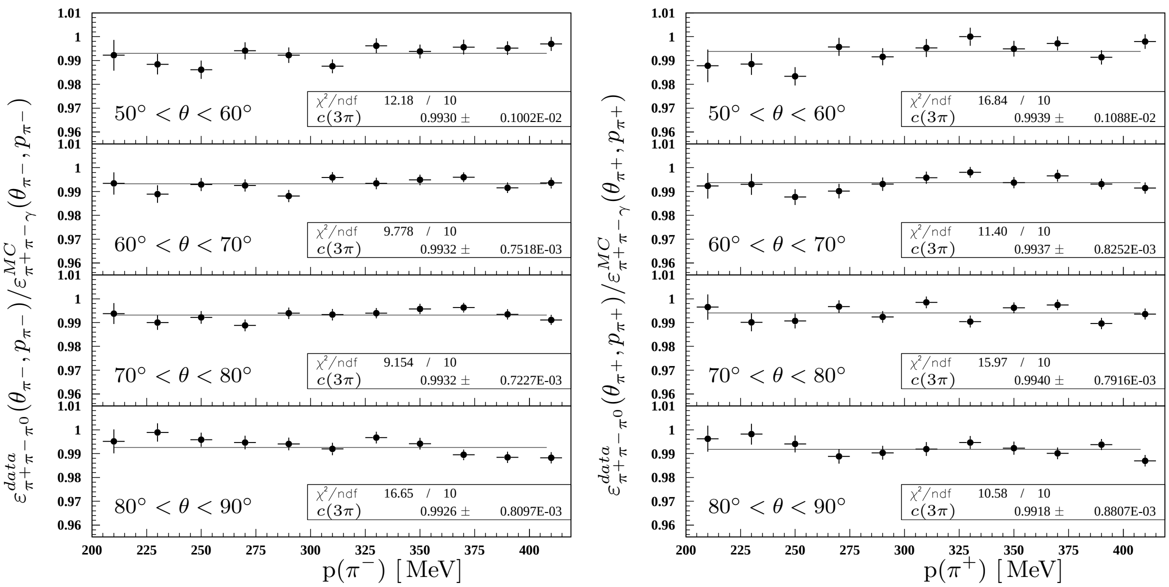

Figure 21: Ratio of the single track efficiency, as a function of momentum, between pions obtained from $\pi^+\pi^-\pi^0$ data and $\pi^+\pi^-\gamma$ MC events. The average ratio over momentum is taken as the data-MC correction for each angle interval indicated inside the panels.

The tracking efficiency as a function of $M^2_{\pi\pi}$ is obtained mapping these single pion efficiencies, measured as a function of p and θ, with generated kinematics from Monte Carlo. In particular, we used events with the same acceptance and M_{trk} cuts of the event selection.

For a given bin in $M^2_{\pi\pi}$ (width $= 0.01\,\text{GeV}^2$), the tracking efficiency is an average over the n different configurations of $(\theta_{\pi^+}, p_{\pi^+}, \theta_{\pi^-}, p_{\pi^-})$ contributing to that bin:

$$\varepsilon_{\text{trk}}(M^2_{\pi\pi}) = \frac{1}{N}\sum_{k=1}^{n} \nu_k \; \varepsilon_k, \tag{4.9}$$

where N is the number of Monte Carlo events used to compute the frequency ν_k with which a certain k configuration occurs.

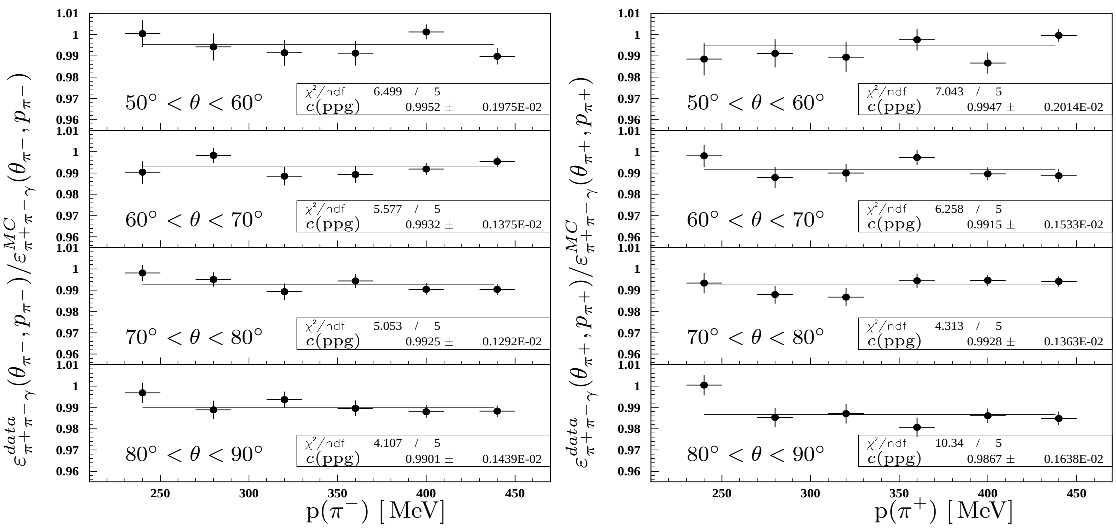

Figure 22: Ratio of the single track efficiency as a function of momentum, between pions obtained from $\pi^+\pi^-\gamma$ data and $\pi^+\pi^-\gamma$ MC events. The average ratio over momentum is taken as the data-MC correction for each angle interval indicated inside the panels.

The correction factors in Fig. 21 (constant as function of momentum) and Fig. 22 has been used to evalute the data-Monte Carlo corrections as function of $M_{\pi\pi}^2$ to the tracking efficiency. The fractional difference between the results obtained with the two samples is 0.3%, which is taken as systematic error.

4.7 Pion cluster identification efficiency

In this analysis, each track is extrapolated to the calorimeter and at least one cluster is searched for within a sphere of radius $|\vec{r}_{ext} - \vec{r}_{\rm clu}| < 90$ cm, where $\vec{r}_{\rm ext}$ and $\vec{r}_{\rm clu}$ are the coordinates of the extrapolated point of the track in the calorimeter and of the cluster centroid, respectively. If there is more than 1 cluster inside this sphere, the most energetic one is defined as the cluster associated to the track.

Fig. 23 shows that the distance between the extrapolated points of the pion tracks is larger than 3 m, for the $M_{\pi\pi}$ region of interest.

Clusters associated to the tracks are used to provide the trigger (see below subsection) and for the purpose of particle identification, by means of the same likelihood function [11] computed for the analysis of the published results, but trained with 2002 data sample. We require at least one track to be identified as a pion, namely at least one track must have an associated cluster with $\log \mathcal{L}_\pi/\mathcal{L}_e > 0$. This requirement is equivalent to exclude events in the low left rectangle of Fig. 24.

The single $\pi^\pm$ efficiency, $\varepsilon_{\rm tcl}$, is defined as the probability of finding a cluster with $\log \mathcal{L}_\pi/\mathcal{L}_e > 0$, conditioned to the presence of the $\pi^\mp$ track. This is evaluated on both

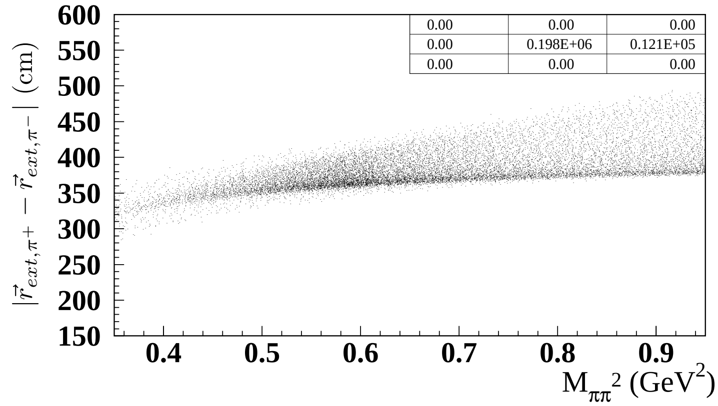

Figure 23: Distance between the points extrapolated to the calorimeter of the 2 pion tracks as a function of invariant mass square of the 2 pions.

data (from a sample of $\sim$ 120 pb^{-1} from "streamed" events) and Monte Carlo (from a sample of $\sim$ 10 pb^{-1} with scale factor 6, *i.e.* effective $\sim$ 60 pb^{-1}) $\pi^+\pi^-\gamma$ events, where the pion track of opposite sign has an associated cluster with $\log \mathcal{L}_\pi/\mathcal{L}_e > 0$ and this fires at least 2 calorimeter trigger sectors.

In this case, the presence of both tracks is exploited in terms of the same $\theta_{\pi\pi} < 15°$ and $M_{\rm trk}$ cuts used in the event analysis of Sec. 3.2, *i.e.* a selection cleaner and more efficient than the control samples obtained from "raw" data for the tracking efficiency.

Therefore, the single pion efficiencies are evaluated in finer slices of momentum (30 bins between 200 and 500 MeV) and polar angle (8 intervals between 50° and 90°) of the fitted pion track, with better resolution than the expected momentum. These are mapped using the formula of eq. 4.9, $\varepsilon_{tcl}(M^2_{\pi\pi}) = (\sum_k \nu_k\ \varepsilon_k)/N$, where (the "OR of the likelihood" is considered) :

$$\varepsilon_k = 1 - \left[1 - \varepsilon^{data}_{\pi^+\pi^-\gamma}(\theta_{\pi^+}, p_{\pi^+})\right]\left[1 - \varepsilon^{data}_{\pi^+\pi^-\gamma}(\theta_{\pi^-}, p_{\pi^-})\right] \quad \rightarrow \quad \varepsilon^{data}_{\pi^+\pi^-\gamma}(M^2_{\pi\pi}) \quad (4.10)$$

$$\varepsilon_k = 1 - \left[1 - \varepsilon^{MC}_{\pi^+\pi^-\gamma}(\theta_{\pi^+}, p_{\pi^+})\right]\left[1 - \varepsilon^{MC}_{\pi^+\pi^-\gamma}(\theta_{\pi^-}, p_{\pi^-})\right] \quad \rightarrow \quad \varepsilon^{MC}_{\pi^+\pi^-\gamma}(M^2_{\pi\pi}) \quad (4.11)$$

The choice of the track-to-cluster association radius $R_{\rm tca} = |\vec{r}_{ext} - \vec{r}_{clu}| = 90$ cm is motivated by trigger studies discussed below. Fig. 25 shows both $\varepsilon^{data}_{\pi^+\pi^-\gamma}(M^2_{\pi\pi})$ and $\varepsilon^{MC}_{\pi^+\pi^-\gamma}(M^2_{\pi\pi})$, depending on $R_{\rm tca} =$ 70, 80, 90, 100, 110 cm.

The ratio, $r90 \equiv \varepsilon^{data}(M^2_{\pi\pi})/\varepsilon^{MC}(M^2_{\pi\pi})$, between data and Monte Carlo efficiencies with $R_{\rm tca} = 90$ cm is used and the relative systematic error is given by the relative difference between $r110$ and $r70$ and results to be $<< 0.1\%$, and is therefore considered negligible.

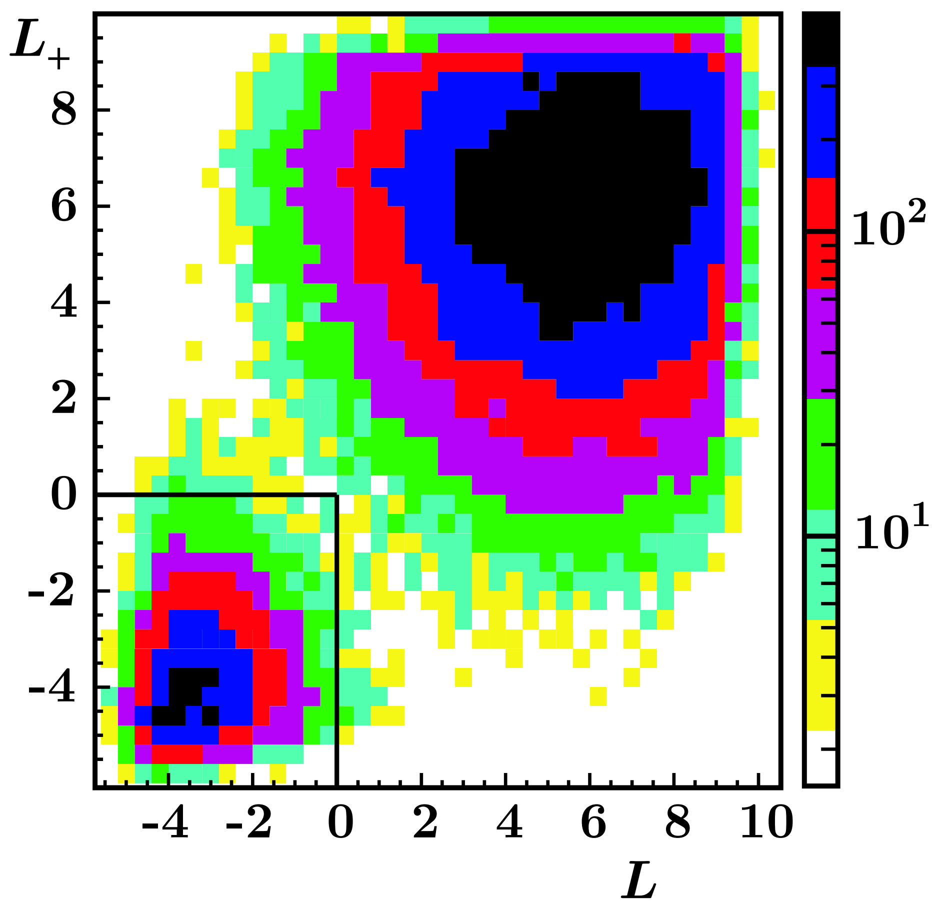

Figure 24: PID distributions for both tracks. Events contained in the low left rectangle are regarded as $e^+e^-\gamma$ events, and rejected in the selection.

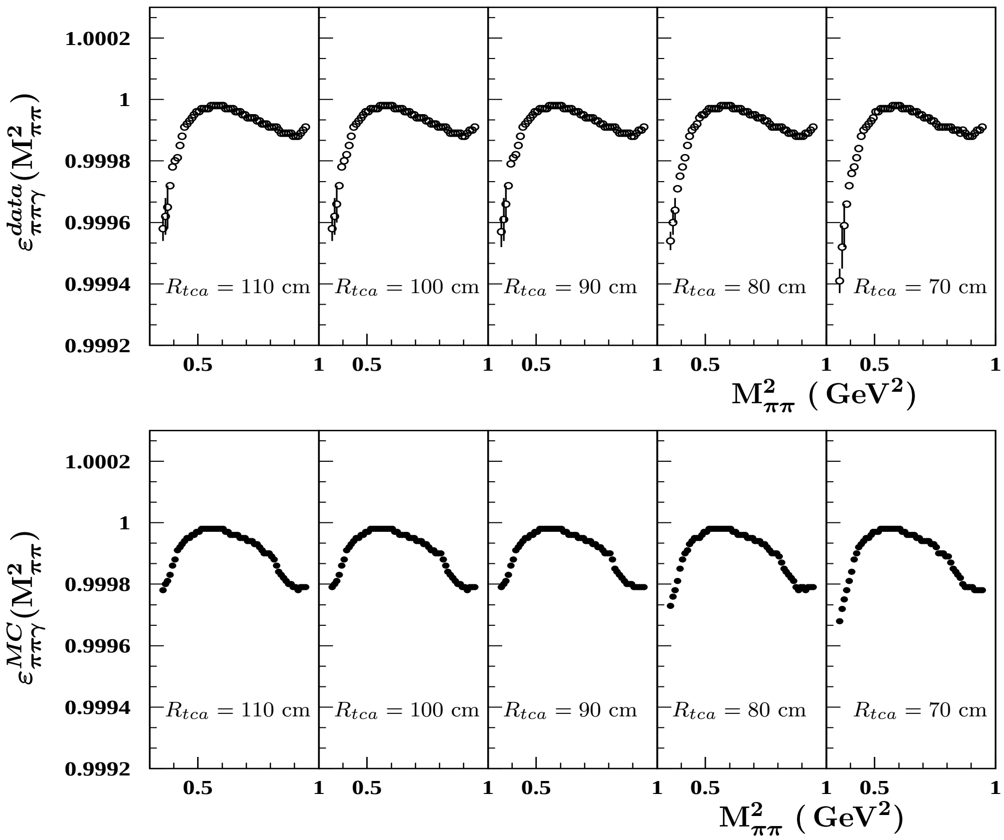

Figure 25: Efficiency of finding at least an associated cluster identified as a pion as a function of the $\pi\pi$ invariant mass, depending on the association radius for $\pi^+\pi^-\gamma$ data (top) and Monte Carlo (bottom) events.

4.8 Trigger corrections

Signal events are selected according to calorimeter *self-triggering* pions: at least two trigger sectors [10] with energy deposit above threshold – provided that they are not located in the same end cap – must be fired by the clusters associated to the pion tracks.

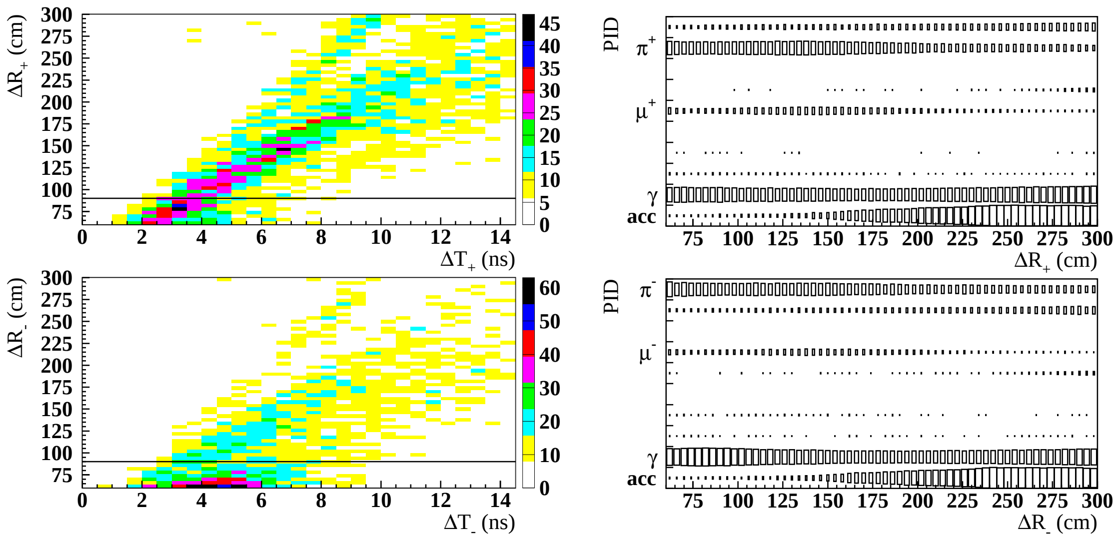

Figure 26: Left: space–time correlation of the clusters able to fire one calorimeter trigger sector with respect to extrapolated point, $\vec{r}_{ext}$, of the positive (top) and the negative (down) pion track, from data. Right: particle identity of the clusters able to fire one calorimeter trigger sector as a function of $\Delta R \equiv |\vec{r}_{clu} - \vec{r}_{ext}|$, for positive (top) and negative (down) pion tracks, from Monte Carlo.

The efficiency for this selection is obtained with the single pion method, from the same samples used in the previous subsection. The two tracks satisfying the requirements of the analysis selection are extrapolated to the calorimeter. Clusters with the centroid located within 90 cm from the point extrapolated from the $\pi^\pm$ track to the calorimeter are assigned to the $\pi^\pm$ category. The choice of 90 cm radius is motivated by the need to include as many clusters originated by pions – either fragments or photons produced in π interactions with the calorimeter – as possible.

Clusters firing 1 sector are investigated in terms of their time difference, $\Delta T_\pm$, with respect to the time of the most energetic cluster close to the extrapolated point $\vec{r}_{ext}$ of the pion and the distance, $\Delta R_\pm$, between the cluster centroid and $\vec{r}_{ext}$: the choice of 90 cm allows to include more clusters correlated in time and space to pions. Left panel of Fig. 26 shows the correlation of these variables for $\pi^+\pi^-\gamma$ data events. This behaviour is also confirmed on $\pi^+\pi^-\gamma$ Monte Carlo events: right panel of Fig. 26 shows the particle identity of the clusters as a function of $\Delta R_\pm$, the choice of 90 cm allows to include more clusters originated by the pions and not to add accidental clusters.

The single $\pi^{\pm}$ probability, $P_{0,1}$, of firing 0 or 1 trigger sectors is measured for both data and MC signal events where the trigger is provided by the $\pi^{\mp}$. This probability is parametrized in 30 momentum bins between 200 and 500 MeV and 8 intervals of polar angle between $50°$ and $90°$ of the pion track.

The self-trigger efficiency as a function of $M_{\pi\pi}^2$ is obtained mapping the single pion probabilities as in eq. 4.9, $\varepsilon_{trg}(M_{\pi\pi}^2) = (\sum_k \nu_k\ \varepsilon_k)/N$, where for both data and MC:

$$\varepsilon_k = 1 - P_1(\theta_+, p_+)P_0(\theta_-, p_-) - P_0(\theta_+, p_+)P_1(\theta_-, p_-) - P_0(\theta_+, p_+)P_0(\theta_-, p_-)\ \rightarrow\ \varepsilon_{\pi\pi\gamma}(M_{\pi\pi}^2) \tag{4.12}$$

The correctness of this combinatorial has been checked by Monte Carlo.

The efficiency evaluated with the single pion method using data is checked with an estimate of the efficiency of self-triggering pions conditioned to the drift chamber trigger.

With the following conventions:

$$\text{N. of events with EMC trigger} = \varepsilon_{\text{EMC}} N_{\text{TOT}} = N_{\text{EMC}}$$
$$\text{N. of events with DC trigger} = \varepsilon_{\text{DC}} N_{\text{TOT}} = N_{\text{DC}}$$
$$\text{N. of events with both triggers} = \varepsilon_{\text{EMC}} \varepsilon_{\text{DC}} C_T N_{\text{TOT}} = N_{\text{BOTH}}$$

C_T is the correlation term between EMC and DC triggers, where $C_T = 1$ means no correlation.

Monte Carlo studies prove that $C_T \approx 1$ for $\pi^+\pi^-\gamma$ events of this analysis.

We applied the ratio of data over Monte Carlo efficiencies, obtained with single pion method of eq. 4.12. The systematic error of the trigger correction is evaluated comparing the single pion method with the DC conditioned efficiency, from the same data sample. Fig. 27 shows the comparison between self-triggering pion efficiencies, evaluated with the two methods. The relative systematic error is about 0.1%.

4.9 From $M_{\pi\pi}^2$ to $(M_{\pi\pi}^0)^2$

The quantity $M_{\pi\pi}^2$ is computed from measured momenta of the pions and is shifted by radiative effects from the mass value at the $\pi^+\pi^-\gamma$ vertex, $(M_{\pi\pi}^0)^2$ (see Fig. 28). The transition from $M_{\pi\pi}^2$ to $(M_{\pi\pi}^0)^2$ is evaluated using a private version of the PHOKHARA Monte Carlo generator [27] . This generator allows to (approximately) tell whether a generated photon comes from the initial or the final state. The presence of final state radiation shifts the observed value of $M_{\pi\pi}^2$ (evaluated from the momenta of the two charged pion tracks in the events) away from the value of the invariant mass squared of the virtual photon produced in the collision of the electron and the positron. The shift is only in one direction, $(M_{\pi\pi}^0)^2 \geq M_{\pi\pi}^2$.

To find out in which bin of $(M_{\pi\pi}^0)^2$ an event with a measured value of $M_{\pi\pi}^2$ belongs, a probability matrix similar to the unfolding matrix in Sec. 4.5 has been constructed (see Fig. 29). As the unshifting correction is performed inside the small angle acceptance cuts ($50^o < \theta_\pi < 130^o$, $\theta_{\pi\pi} < 15^0$ or $\theta_{\pi\pi} > 165^0$), the effect of this correction (which is necessitated by the presence of final state radiation in the selected events) is minimized due to the natural suppression of events with final state radiation for these acceptance cuts.

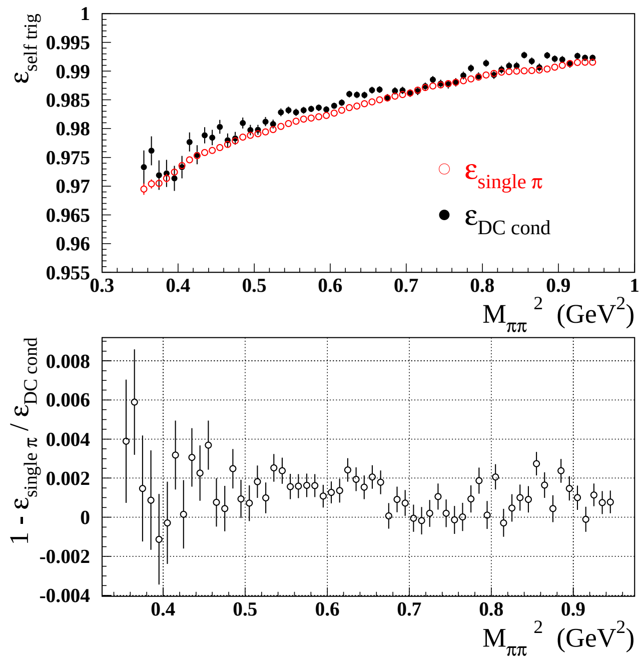

Figure 27: Top: comparison between the single pion method and the efficiencies for self-triggering pions obtained from events with a drift chamber trigger as a function of the $\pi\pi$ invariant mass, obtained from the same data sample. Down: the relative difference.

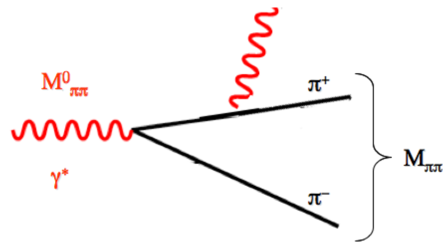

Figure 28: Photon emission from pions, shifting the dipion mass $M^0_{\pi\pi} \to M_{\pi\pi}$.

A matrix multiplication similar to the one used to estimate the systematic uncertainty in the unfolding procedure is then applied to *unshift* the spectrum and pass from $M^2_{\pi\pi}$ to $(M^0_{\pi\pi})^2$.

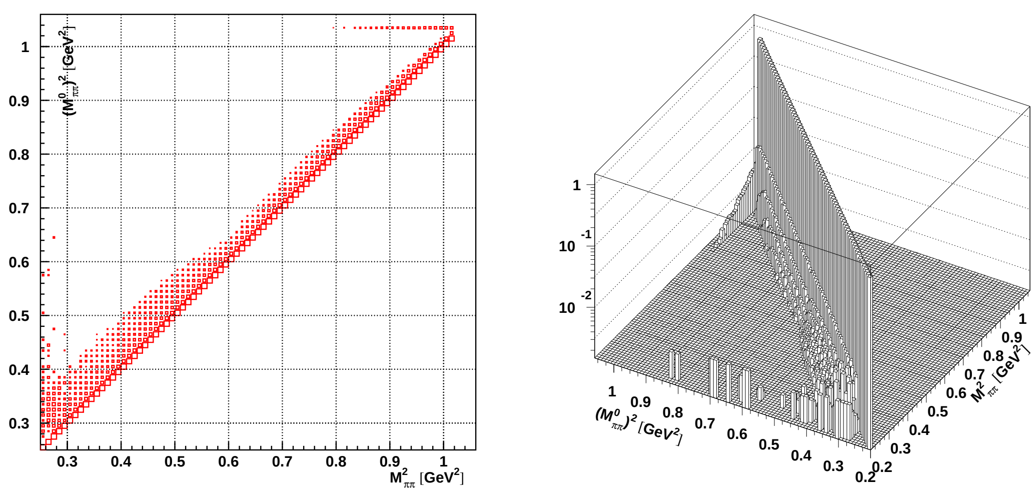

Figure 29: Unshifting matrix. The line above $(M^0_{\pi\pi})^2 = 1.03$ GeV^2 in the left plot represents events with two pions and one photon in the final state. As our final results extend only up to $(M^0_{\pi\pi})^2 = 0.95$ GeV^2, these events are outside the range.

Fig. 30, obtained directly from Monte Carlo, shows the unshifting correction on the spectrum. The relative increase of final state radiation due to events with one photon from ISR and one photon from FSR over pure ISR events at low values of $M^2_{\pi\pi}$ introduces a larger effect of the unshifting in this region, resulting in a decrease of the spectrum in this region (for a more detailed discussion on the unshifting, see [28]).

4.10 Acceptance

The acceptance for the cuts in θ_π and $\theta_{\pi\pi}$ for $\sigma_{\pi\pi}$ and $|F_\pi|^2$ are evaluated using the private version of the PHOKHARA Monte Carlo generator which has also been used in Sec. 4.9, as they need to be known in bins of $(M^0_{\pi\pi})^2$, the invariant mass squared of the virtual photon

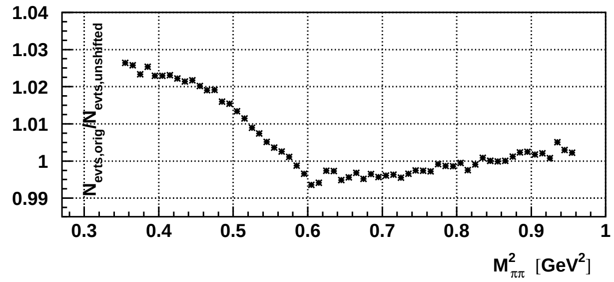

Figure 30: Unshifting correction due to final state radiation on the spectrum (obtained from Monte Carlo).

produced in the collision of the electron and the positron[3]. To exclude the doublecounting of acceptances, the acceptance in θ_π has been evaluated for events with $\theta_{\pi\pi} < 15^0$ or $\theta_{\pi\pi} > 165^0$.

Fig. 31 shows the acceptance for the cut in $50^o < \theta_\pi < 130^o$ (left) and $\theta_{\pi\pi} < 15^0$ or $\theta_{\pi\pi} > 165^0$ (right).

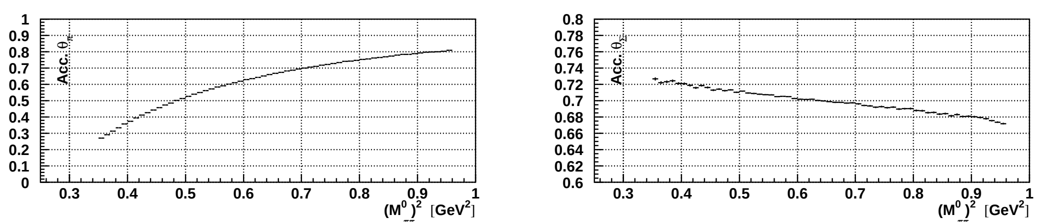

Figure 31: Left: Acceptance for the cut in θ_π (conditioned to the cut on $\theta_{\pi\pi}$). Right: Acceptance for the cut in $\theta_{\pi\pi}$.

4.10.1 Systematic error on Acceptance

We evaluated the fractional difference in the $M^2_{\pi\pi}$ spectrum for both data and Monte Carlo, varying the cut (see Fig 32) $\theta_{\pi\pi} < \theta_{\text{cut}} = 15°$ (or $\theta_{\pi\pi} > \theta_{\text{cut}} = 15°$).

If $\theta_{\text{cut}} < 15°$ (*e.g.* selecting events with $\theta_{\pi\pi} < 14°$) we evaluated the quantity:

$$\frac{N(\theta_{\pi\pi} < \theta_{\text{cut}}) - N(\theta_{\pi\pi} < 15°)}{N(\theta_{\pi\pi} < 15°)} = \frac{N(\theta_{\pi\pi} < \theta_{\text{cut}})}{N(\theta_{\pi\pi} < 15°)} - 1 = -\frac{N(\theta_{\text{cut}} < \theta_{\pi\pi} < 15°)}{N(\theta_{\text{cut}} < \theta_{\pi\pi} < 15°) + N(\theta_{\pi\pi} < \theta_{\text{cut}})} \tag{4.13}$$

where the third expression focuses on the independent quantities and provides the correct statistical error propagation

$$\frac{\sqrt{N^2(\theta_{\text{cut}} < \theta_{\pi\pi} < 15°)\, N(\theta_{\pi\pi} < \theta_{\text{cut}}) + N(\theta_{\text{cut}} < \theta_{\pi\pi} < 15°)\, N^2(\theta_{\pi\pi} < \theta_{\text{cut}})}}{[N(\theta_{\text{cut}} < \theta_{\pi\pi} < 15°) + N(\theta_{\pi\pi} < \theta_{\text{cut}})]^2} \tag{4.14}$$

[3]As the differential cross section $d\sigma_{\pi\pi\gamma}/dM^2_{\pi\pi}$ is not corrected for the transition from $M^2_{\pi\pi}$ to $(M^0_{\pi\pi})^2$, the acceptance correction in $\theta_{\pi\pi}$ in this case is done in $M^2_{\pi\pi}$.

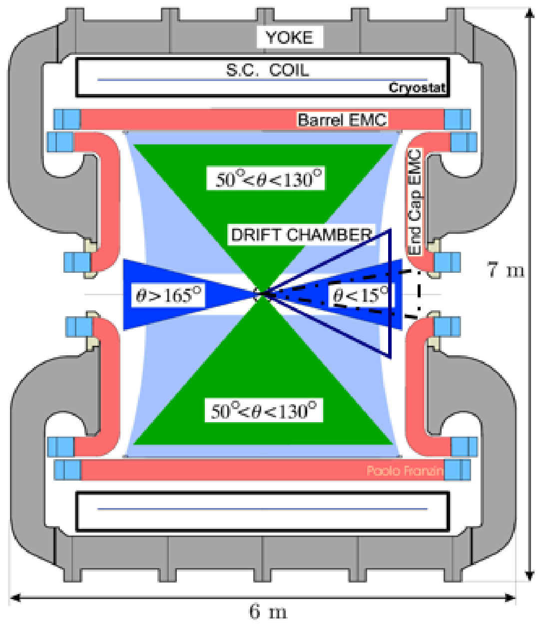

Figure 32: Fiducial volume of the analysis, together with enlarging (or squeezing) of the $\theta_{\pi\pi}$ cone. Both hemispheres are considered in the analysis and in these studies.

If $\theta_{\rm cut} > 15°$ (*e.g.* selecting events with $\theta_{\pi\pi} < 16°$) we evaluated the quantity:

$$\frac{N(\theta_{\pi\pi} < \theta_{\rm cut}) - N(\theta_{\pi\pi} < 15°)}{N(\theta_{\pi\pi} < 15°)} = \frac{N(\theta_{\pi\pi} < \theta_{\rm cut})}{N(\theta_{\pi\pi} < 15°)} - 1 = \frac{N(15° < \theta_{\pi\pi} < \theta_{\rm cut})}{N(\theta_{\pi\pi} < 15°)} \tag{4.15}$$

We measured how well the Monte Carlo reproduces the acceptance cut on data, in a way similar to the studies for the acceptance in the luminosity measurement [29].

Fig. 34 and Fig. 35 show the fractional variation on the $M^2_{\pi\pi}$ spectrum as a function of $\theta_{\rm cut}$.

The excursion on the spectrum at $\theta_{\rm cut} = (15 \pm 1)°$ as function of $M^2_{\pi\pi}$ is taken as systematic error.

The systematic errors are given in Table 4.

$M^2_{\pi\pi}$ range (GeV^2)	Systematic error (%)
$0.35 \leq M^2_{\pi\pi} < 0.39$	0.6
$0.39 \leq M^2_{\pi\pi} < 0.43$	0.5
$0.43 \leq M^2_{\pi\pi} < 0.45$	0.4
$0.45 \leq M^2_{\pi\pi} < 0.49$	0.3
$0.49 \leq M^2_{\pi\pi} < 0.51$	0.2
$0.51 \leq M^2_{\pi\pi} < 0.64$	0.1
$0.64 \leq M^2_{\pi\pi} < 0.95$	-

Table 4: Acceptance systematic errors.

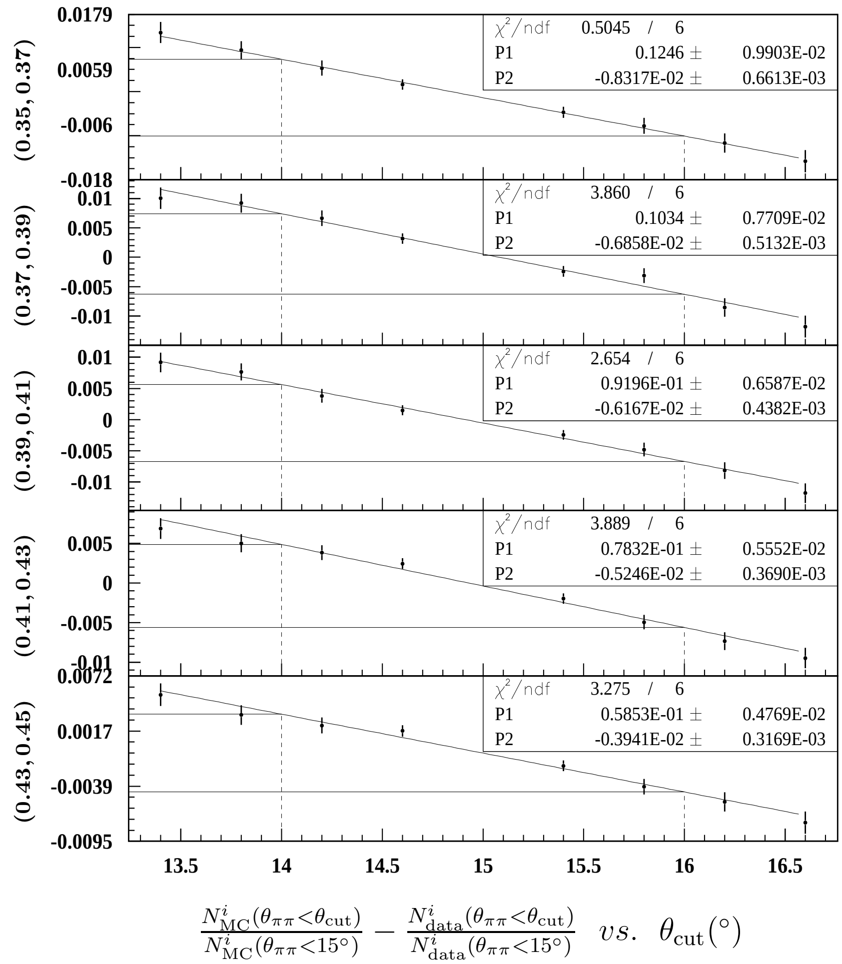

Figure 33: Dependence on $\theta_{\rm cut}$ with increasing $M^2_{\pi\pi}$ ranges from upper to lower panels. These ranges (in $\rm GeV^2$) are specified in the plot in place of the ordinate labels.

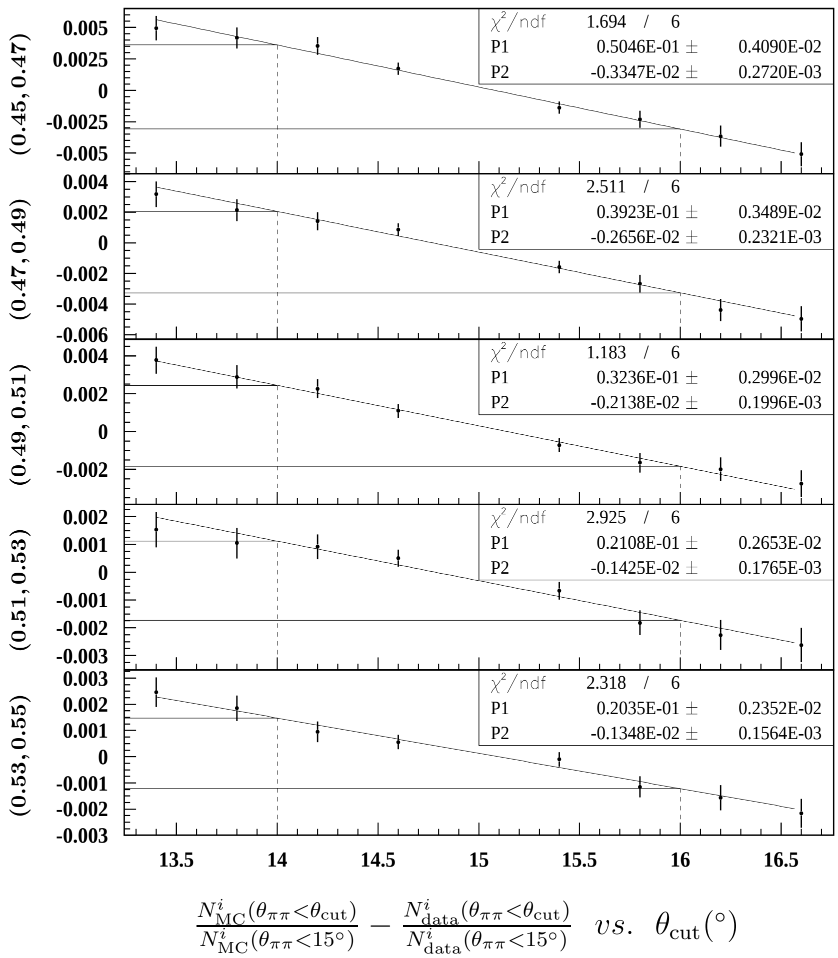

Figure 34: Dependence on $\theta_{\rm cut}$ with increasing $M^2_{\pi\pi}$ ranges from upper to lower panels. These ranges (in GeV^2) are specified in the plot in place of the ordinate labels.

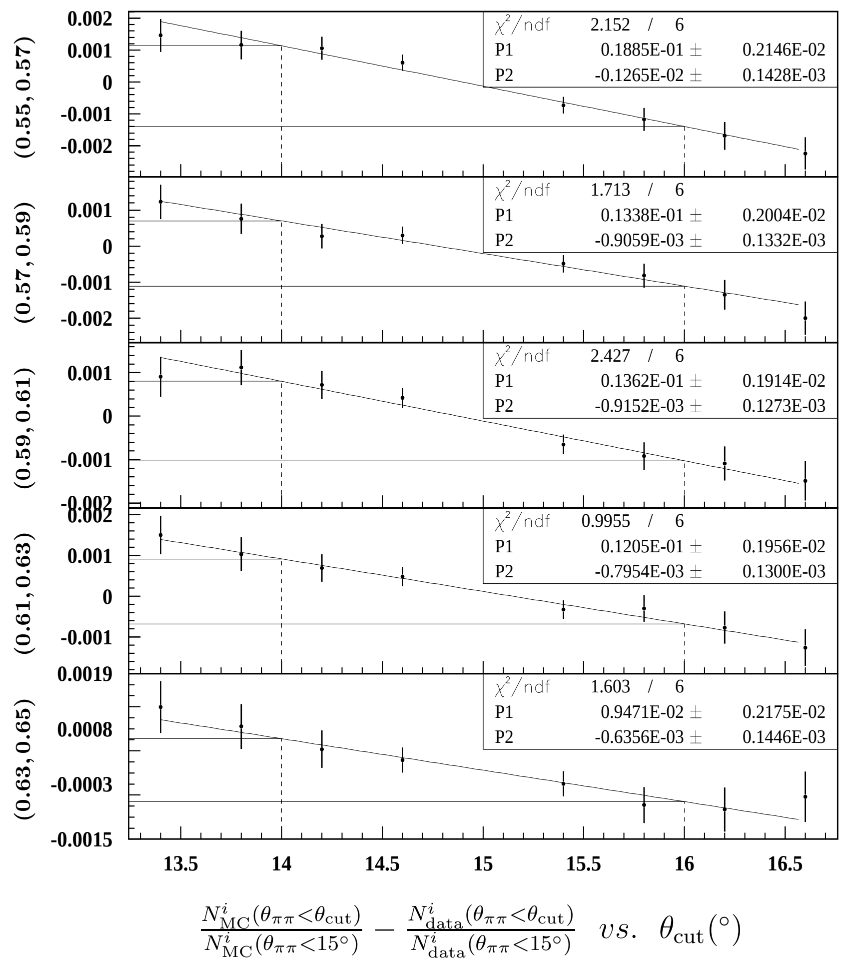

Figure 35: Dependence on $\theta_{\rm cut}$ with increasing $M^2_{\pi\pi}$ ranges from upper to lower panels. These ranges (in GeV^2) are specified in the plot in place of the ordinate labels.

4.11 Luminosity

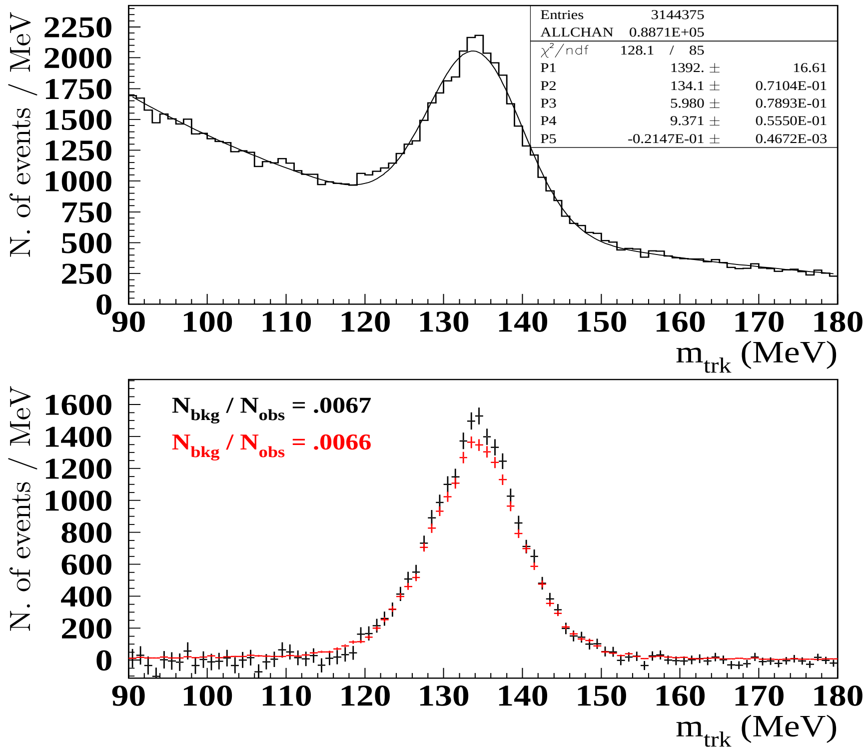

Figure 36: Top: zoom of $M_{\rm trk}$ spectrum from VLAB data fitted with the sum of an exponential plus a Gaussian functions. Down: the same spectrum, after subtracting the exponential, compared with a distribution of events with both tracks identified as pions, from the same data sample.

The absolute normalization of the data sample is obtained [30] from very large angle ($55^\circ < \theta < 125^\circ$) Bhabha, VLAB, events. The integrated luminosity, $\mathcal{L}$, is provided by:

$$\mathcal{L} = \frac{N_{\rm obs} - N_{\rm bkg}}{\sigma_{\rm eff}} \; , \tag{4.16}$$

where $N_{\rm obs}$ is the number of candidate large angle Bhabha events, $N_{\rm bkg}$ is the number of background events and $\sigma_{\rm eff}$ is the effective cross section for the KLOE VLAB selection cuts. This is cross section is evaluated by the Monte Carlo generator `Babayaga` [31] – including QED radiative corrections with the parton shower algorithm – interfaced with the KLOE detector simulation `GEANFI` [7]. The method for the luminosity determination, the event-selection criteria, and the systematics are all discussed in [30], and we consider here only the updates for the 2002 data analysis.

An updated version of the generator, `Babayaga@NLO` [32], has been released, in which the new predicted cross section decreases by 0.7% ($\sigma_{Bhabha} = 456.2\ nb$) [4] and the theoretical uncertainty improves from 0.5% to 0.1% with respect to the older version.

From the experimental point of view, the hardware veto of cosmic rays, has been removed during 2002 data taking. This implies that this inefficiency is not present in this analysis of VLAB events, and, furthermore, the background process $e^+e^- \to \pi^+\pi^-$ is slightly increased with respect to the analysis of 2001 data, because the veto inefficiency was remarkable for this class of events.

Fig. 36, top, shows the tail of the $M_{\rm trk}$ spectrum of VLAB events in which the signal and background distributions are respectively parametrized with an exponential and a Gaussian function. Fig. 36, bottom, shows the comparison of the same spectrum after subtracting the exponential with the distribution of events with both tracks fulfilling the pion identification $-\log \mathcal{L}_\pi/\mathcal{L}_e > 0$ – out of the same sample.

Table 5 lists the differences in the contributions to the corrections and systematic errors used for the luminosity measurement, between the analyses of the two data sets.

	2001	2002
relative theoretical error on $\sigma_{\rm eff}$	0.5%	0.1%
background correction	−0.6%	−0.7%
cosmic ray veto efficiency	+0.4%	negligible
relative error on $\mathcal{L}$: $\delta_{th} \oplus \delta_{exp}$	0.6%	0.3%

Table 5: Differences between 2001 and 2002 corrections and systematic errors on the luminosity measurement.

More in detail, the background correction is the fraction of events identified as $e^+e^- \to \pi^+\pi^-$ to be subtracted from data and cosmic ray veto efficiency is the fraction of events to be added to the event counts, because of this inefficiency. The relative systematic error on the luminosity measurement is 0.3%.

5 Radiative corrections

5.1 The radiator function

To pass from the radiative differential cross section

$$\mathrm{d}\sigma(e^+e^- \to \pi\pi + \gamma_{\rm ISR}(\gamma_{\rm ISR}))(M^2_{\pi\pi}, \theta_{\pi\pi})/\mathrm{d}M^2_{\pi\pi}$$

to the total cross section for the process $e^+e^- \to \pi^+\pi^-$, in the absence of photons from final state radiation, one can relate the two items by introducing a theoretical radiator function $H(M^2_{\pi\pi}, s, \theta_{\pi\pi})$ via the equation [8, 33]

$$\frac{\mathrm{d}\sigma(e^+e^- \to \pi\pi + \gamma_{\rm ISR}(\gamma_{\rm ISR}))(M^2_{\pi\pi}, \theta_{\pi\pi})}{\mathrm{d}M^2_{\pi\pi}} \times s = H(M^2_{\pi\pi}, s, \theta_{\pi\pi}) \times \sigma(e^+e^- \to \pi\pi)(M^2_{\pi\pi}) \tag{5.1}$$

[4]For a comparison of the Bhabha cross section with the other generators see [30].

Here $M^2_{\pi\pi}$ is the squared invariant mass of the two-pion system (which is identical to the squared invariant mass of the virtual photon γ^* in the absence of FSR), s is the squared center-of-mass energy of the DAΦNE collider, and $\theta_{\pi\pi}$ is the angle of the photon or the photon system (in case there is more than one photon). The dimensionless quantity H describes the emission of soft, virtual and hard photons in the initial state.

Using $\sigma_{\pi\pi}(M^2_{\pi\pi}) = \frac{\pi\alpha^2}{3M^2_{\pi\pi}}\beta^3_\pi|F_\pi(M^2_{\pi\pi})|^2$, one can easily rewrite eq. 5.1 as[5]

$$\frac{\mathrm{d}\sigma_{\pi\pi\gamma(\gamma)}(M^2_{\pi\pi},\theta_{\pi\pi})}{\mathrm{d}M^2_{\pi\pi}} = \frac{H(M^2_{\pi\pi},s,\theta_{\pi\pi})}{s} \times \frac{\pi\alpha^2}{3M^2_{\pi\pi}}\beta^3_\pi|F_\pi(M^2_{\pi\pi})|^2 \tag{5.2}$$

One can exploit eq. 5.2 using the PHOKHARA Monte Carlo generator, which contains ISR processes to next-to-leading order [33], to obtain the H-function. Setting $|F_\pi(M^2_{\pi\pi})|^2 = 1$ in the generator (and switching off the vacuum polarization of the intermediate photon in the generator), $H(M^2_{\pi\pi},s,\theta_{\pi\pi})$ becomes

$$H(M^2_{\pi\pi},s,\theta_{\pi\pi}) = s \times \frac{3M^2_{\pi\pi}}{\pi\alpha^2\beta^3_\pi} \times \frac{\mathrm{d}\sigma_{\pi\pi\gamma(\gamma)}(M^2_{\pi\pi},\theta_{\pi\pi})}{\mathrm{d}M^2_{\pi\pi}}\Big|^{MC}_{|F_\pi(M^2_{\pi\pi})|^2=1} \tag{5.3}$$

This is a convenient mechanism to extract H for certain cut values of θ_Σ without having to deal with analytic formulas. If the binwidth $\mathrm{d}M^2_{\pi\pi}$ is chosen identical for the measured $\frac{\mathrm{d}\sigma_{\pi\pi\gamma(\gamma)}}{\mathrm{d}M^2_{\pi\pi}}$ and the $\frac{\mathrm{d}\sigma_{\pi\pi\gamma(\gamma)}}{\mathrm{d}M^2_{\pi\pi}}\Big|^{MC}_{|F_\pi(M^2_{\pi\pi})|^2=1}$ obtained from Monte Carlo, the division for H automatically passes from a differential to an absolute cross section.

In the present analysis, H is evaluated for $0^\circ < \theta_{\pi\pi} < 180^\circ$, as shown in Fig. 37. Using a radiator function which is inclusive in $\theta_{\pi\pi}$ allows to factorize and treat consistently FSR effects in the evaluation of the $\theta_{\pi\pi}$ acceptance (see Sec. 5.2).

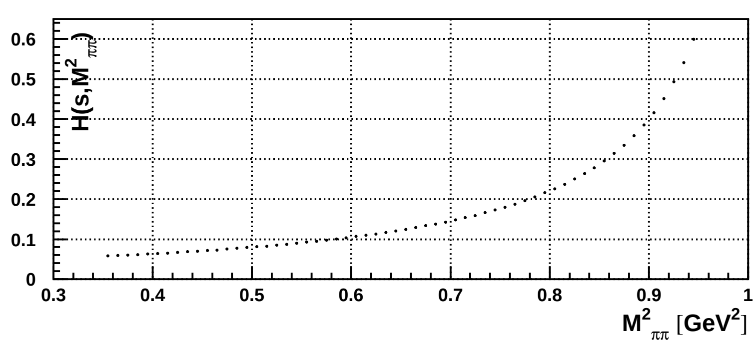

Figure 37: The dimensionless radiator function $H(M^2_{\pi\pi},s)$, inclusive in θ_Σ, in bins of 0.01 GeV^2 in $M^2_{\pi\pi}$. The value used for s in the Monte Carlo production is $s = (M_\phi)^2 = (1.019456\ GeV)^2$

.

[5] $\beta_\pi = \sqrt{1 - \frac{4m^2_\pi}{M^2_{\pi\pi}}}$

5.1.1 Systematic error of the radiator function

The error quoted by the authors of PHOKHARA on the ISR part of the generator is 0.5%, mainly due to missing diagrams like non-factorizable two-photon exchange graphs (see Fig. 38).

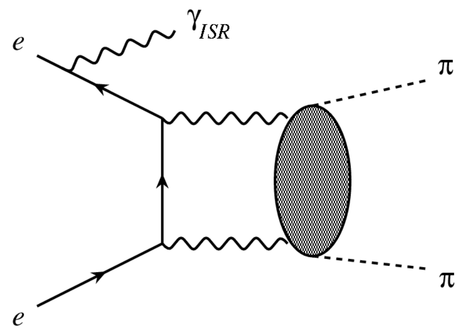

Figure 38: Two-photon exchange graph, not simulated in PHOKHARA.

In addition, we add an experimental systematic uncertainty to the radiator function due to the spread of $\sqrt{s}$ during the 2002 running period of DAΦNE. Fig. 39, left, shows the spread in $\sqrt{s}$ in the data. Fig. 39, right, shows the ISR cross section $\frac{d\sigma_{\pi\pi\gamma}}{dM_{\pi\pi}^2}\Big|^{MC}_{|F_\pi(M_{\pi\pi}^2)|^2=1}$ for two extreme values of $\sqrt{s}$ (1019.2 and 1019.8 GeV), divided by the corresponding value of s (as one needs to divide the measured cross section for H/s, see eq. 5.2). The experimental systematic uncertainty is taken as half of the relative difference between the cross sections in Fig. 39, right. Fig. 40 and Table 6 show the relative systematic uncertainty on H coming from the spread in $\sqrt{s}$. This introduces an error of 0.2% on the value of $a_\mu^{\pi\pi}$.

$(M^0_{\pi\pi})^2$ (GeV^2)	0.005	0.015	0.025	0.035	0.045	0.055	0.065	0.075	0.085	0.095
0.3						0.3	0.4	0.2	0.1	0.2
0.4	0.1	0.2	0.1	0.2	0.1	0.2	0.2	0.3	0.1	0.2
0.5	0.3	0.3	0.1	0.2	0.3	0.3	0.3	0.2	0.2	0.3
0.6	0.1	0.3	0.3	0.2	0.2	0.3	0.3	0.3	0.2	0.3
0.7	0.3	0.3	0.4	0.3	0.3	0.3	0.4	0.3	0.3	0.3
0.8	0.4	0.4	0.3	0.5	0.4	0.5	0.4	0.4	0.5	0.5
0.9	0.5	0.6	0.6	0.6	0.7					

Table 6: Systematic error in % due to the the spread in $\sqrt{s}$ in the 2002 data taking period, given in 0.01 GeV^2 bin intervals of $(M^0_{\pi\pi})^2$. The bin center is given by the sum of the values in the first row and first column.

5.2 The treatment of final state radiation

The presence of events with final state radiation in the data sample affects our analysis in the following items:

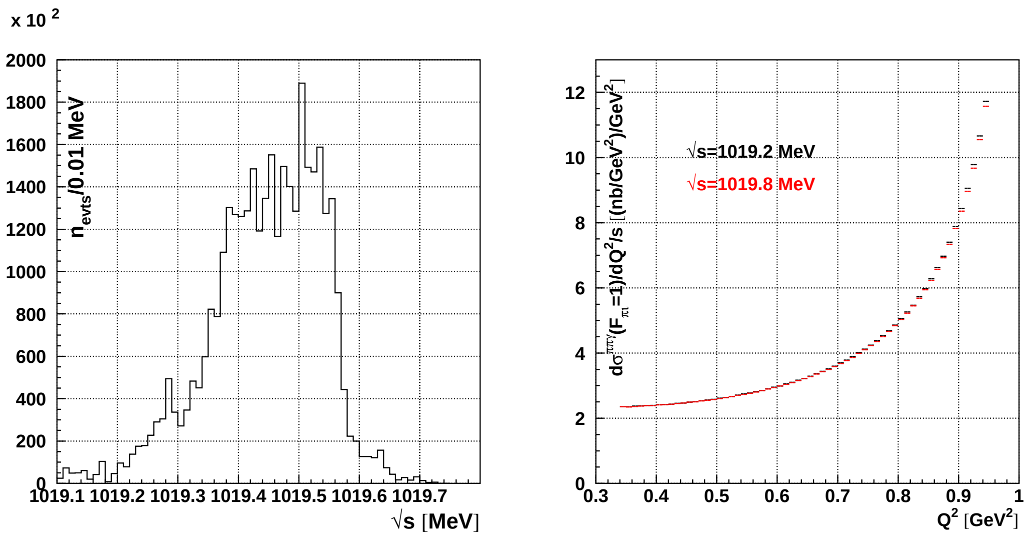

Figure 39: Left: Spread of $\sqrt{s}$ in the data. Right: The ISR-cross section $\left.\frac{\mathrm{d}\sigma_{\pi\pi\gamma}}{\mathrm{d}M^2_{\pi\pi}}\right|^{MC}_{|F_\pi(M^2_{\pi\pi})|^2=1}$ divided by s for two values of $\sqrt{s}$.

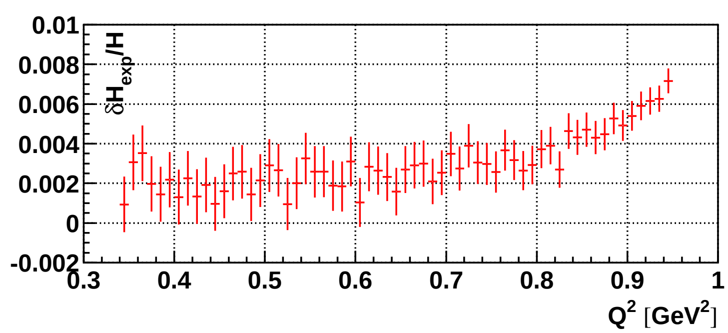

Figure 40: The relative systematic uncertainty on H coming from the spread in $\sqrt{s}$.

- The $M_{\rm trk}$ distributions (Secs. 4.3 and 4.4). These distributions are affected by final state radiation. Missing FSR terms and the model dependence might affect our background fitting procedure and the $M_{\rm trk}$ efficiency. However, as these corrections are performed within the small angle selection cuts, in which FSR is suppressed; and due to the fact that we have found parametrizations which make the Monte Carlo distributions in $M_{\rm trk}$ resemble very much the ones for data (see appendix B for details), we do not expect a non-negligible uncertainty due to final state radiation effect on $M_{\rm trk}$
- The unshifting procedure 4.9. Again, this correction is performed inside the small angle acceptance cuts, minimizing its impact. Still, the correction reaches several

percent at lower values of $(M^0_{\pi\pi})^2$. It has been argued [34] that the presence of a second photon from FSR could give a non-negligible effect, as these higher-order diagrams are not yet included in the PHOKHARA Monte Carlo code. As this is however a higher order effect, we do not expect a sizable contribution.

- The $\theta_{\pi\pi}$ variable. While θ_π is rather unaffected by the presence of final state radiation, this is not true for $\theta_{\pi\pi}$. In fact, the requirement to have $\theta_{\pi\pi}$ at small angles is the key factor for the suppression of final state radiation in this analysis. After correcting for the $\theta_{\pi\pi}$ acceptance, the spectrum is inclusive in $\theta_{\pi\pi}$ and therefore also inclusive with respect to final state radiation. Here we completely depend on the PHOKHARA Monte Carlo generator and the model of photon radiation from pointlike pions (sQED).
- The division for the radiator function $H(s)$. Here we assume factorization between the ISR and the FSR process. This has been tested in the previous publication [6,28], and our assumption was found to be valid within 0.2%.

As all the effects of final state radiation have already been evaluated in our previous publication [6], and since the general approach in this analysis has not changed so much concerning the treatment of final state radiation, we assume the combined error of 0.3% for the uncertainty on the relative FSR contribution and the model dependence to be valid also in this analysis.

5.3 The vacuum polarisation

In order to obtain the *bare* cross section, vacuum polarization effects must be subtracted. This is done by correcting the cross section for the running of α_{em} as follows:

$$\sigma_{bare} = \sigma_{dressed} \left(\frac{\alpha(0)}{\alpha(s)} \right)^2 \equiv \sigma_{dressed}/\delta(s) \tag{5.4}$$

where the running of α can be written as [35]:

$$\alpha(s) = \frac{\alpha(0)}{1 - \Delta\alpha_{lep}(s) - \Delta\alpha_{had}(s)} \tag{5.5}$$

The leptonic contribution can be calculated analytically, while the hadronic contribution comes from a dispersion integral which includes the hadronic cross section itself as integrand[6]:

$$\Delta\alpha_{had}(s) = -\frac{\alpha(0)s}{3\pi} Re \int_{4m_\pi^2}^{\infty} ds' \frac{R(s')}{s'(s' - s - i\epsilon)} \tag{5.6}$$

Therefore, the correct procedure has to be iterative and it should include the same data that must be corrected. However, since the correction is at the few percent level, we have used the $\Delta\alpha_{had}(s)$ as evaluated using $\sigma_{had}(s)$ values measured previously [36].

Fig. 41 shows the correction $\delta(s)$ applied to the $\pi^+\pi^-$ cross section. This correction avoids doublecounting of higher order terms in the dispersion integral for $a_\mu^{\pi\pi}$, and it is not applied to the pion form factor $|F_\pi|^2$ in Table 6 (see also the analysis flow in Fig. 4).

A table with the values of $\delta(s)$ can be found in appendix C. The error on the $\delta(s)$ points adds a systematic contribution to the value of $a_\mu^{\pi\pi}$ of 0.1%.

[6] $R(s) \equiv \sigma^{had}_{bare}(s)/\frac{4\pi\alpha(0)^2}{3s}$

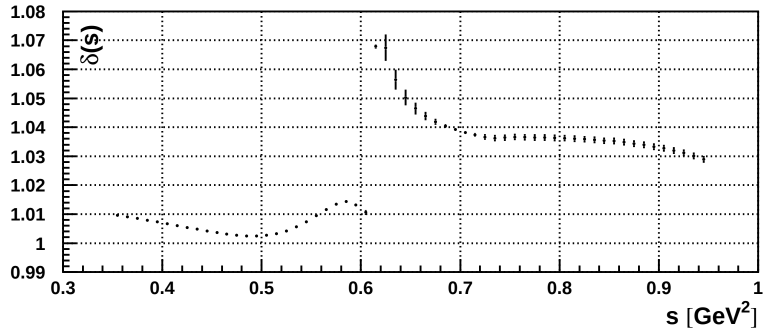

Figure 41: Correction factor $\delta(s)$: $\sigma_{undressed}(s) = \sigma_{dressed}(s)/\delta(s)$, obtained from [36].

6 Results

The differential $\pi^+\pi^-\gamma$ cross section is obtained from the observed count, N_{obs}, after subtracting the residual background, N_{bkg}, correcting for the overall acceptance, $\varepsilon_{\rm acc}(M^2_{\pi\pi})$, and the luminosity $\mathcal{L}$, as discussed in the previous sections:

$$\frac{{\rm d}\sigma_{\pi\pi\gamma}}{{\rm d}M^2_{\pi\pi}} = \frac{N_{\rm obs} - N_{\rm bkg}}{\Delta M^2_{\pi\pi}} \frac{1}{\varepsilon_{\rm acc}(M^2_{\pi\pi})\ \mathcal{L}} \tag{6.1}$$

The differential cross section is then divided by the radiator function (provided by the Phokhara Monte Carlo program [33]) to obtain the measured total cross section $\sigma_{\pi\pi(\gamma)}(M^0_{\pi\pi})^2$, as in eq. 5.1.

The pion form factor can then be obtained from the total cross section $\sigma_{\pi\pi(\gamma)}(M^0_{\pi\pi})^2$ by subtracting FSR under the assumption of pointlike pions (η_{FSR} [37]), and including the effects from vacuum polarisation δ_{VP} (see Sec. 5.3):

$$|F_\pi((M^0_{\pi\pi})^2)|^2 = \frac{3}{\pi}\frac{(M^0_{\pi\pi})^2}{\alpha^2_{em}\ \beta^3_\pi}\sigma_{\pi\pi(\gamma)}\,(1. - \eta_{\rm FSR})\cdot\delta_{VP}. \tag{6.2}$$

Our results are summarized in Table 6, which lists:

- the differential cross section $d\sigma(e^+e^- \to \pi^+\pi^-\gamma)/dM^2_{\pi\pi}$ as a function of the invariant mass of the di-pion system, $M^2_{\pi\pi}$, in the angular region $\theta_{\pi\pi} < 15°$ or $\theta_{\pi\pi} > 165°$, $0° < \theta_\pi < 180°$;
- the *bare* cross section $\sigma(e^+e^- \to \pi^+\pi^-)$, inclusive of FSR, but with the vacuum polarization effects removed [36], as a function of $(M^0_{\pi\pi})^2$;
- the pion form factor dressed with vacuum polarization, but with FSR effects excluded, as a function of $(M^0_{\pi\pi})^2$ (equal to $M^2_{\pi\pi}$ in the absence of FSR).

The cross section for $e^+e^-\to\pi^+\pi^-\gamma$, after applying the corrections described above, is shown in Fig. 42 left, for $|\cos\theta_\gamma| > \cos(15°)$, while the *bare* cross section for $e^+e^- \to \pi^+\pi^-$ is shown in the right panel.

	$\sigma_{\pi\pi\gamma}$	$\sigma_{\pi\pi}^{bare}$	$\vert F_\pi\vert^2$
Reconstruction Filter	negligible		
Background subtraction	$M^2_{\pi\pi}$ dependent (Tab. 2)		
Trackmass	0.2 % flat in $M^2_{\pi\pi}$		
Particle ID	negligible		
Tracking	0.3 % flat in $M^2_{\pi\pi}$		
Trigger	0.1 % flat in $M^2_{\pi\pi}$		
Unfolding	$M^2_{\pi\pi}$ dependent (Tab. 3)		
Acceptance	$M^2_{\pi\pi}$ dependent (Tab 4)		
L3	0.1 % flat in $M^2_{\pi\pi}$		
Luminosity	0.3 % flat in $M^2_{\pi\pi}$		
FSR resummation	-	0.3 %	
Rad. function ($H(M^2_{\pi\pi})$)	-	0.5 %	
$\sqrt{s}$ dep. of H	-	$M^2_{\pi\pi}$ dependent (Tab. 6)	
Vacuum Polarization	-	(Tab. 11)	-

Table 7: List of systematic uncertainties.

The errors given in Table 6 are statistical only, while the common systematic errors are shown in Table 7. It should be noted that the statistical errors account only for the diagonal elements of the covariance matrix. The bin-by-bin errors are correlated as a result of the unfolding procedure; for error propagation, as for example in the calculation of $\Delta^{\pi\pi}a_\mu$ (see below), the covariance matrix must be used [38].

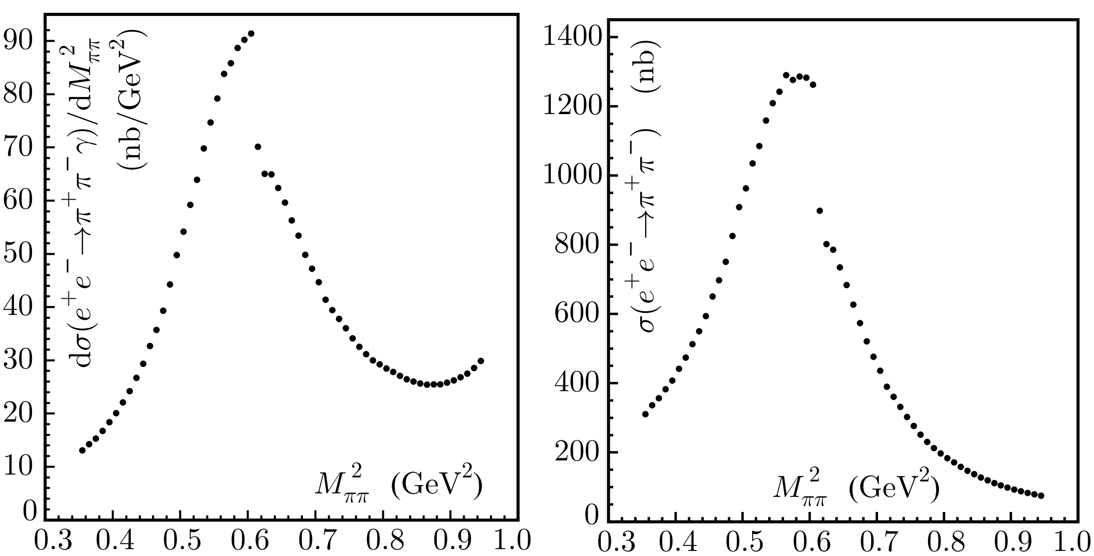

Figure 42: Left: Cross section for the $e^+e^- \to \pi^+\pi^-\gamma(\gamma)$ process, inclusive in θ_π and with $0^o < \theta_{\pi\pi} < 15^o$ or $165^o < \theta_{\pi\pi} < 180^o$. Right: *Bare* cross section for $e^+e^- \to \pi^+\pi^-$.

In Fig. 43, the result for the pion form factor (including vacuum polarisation, and

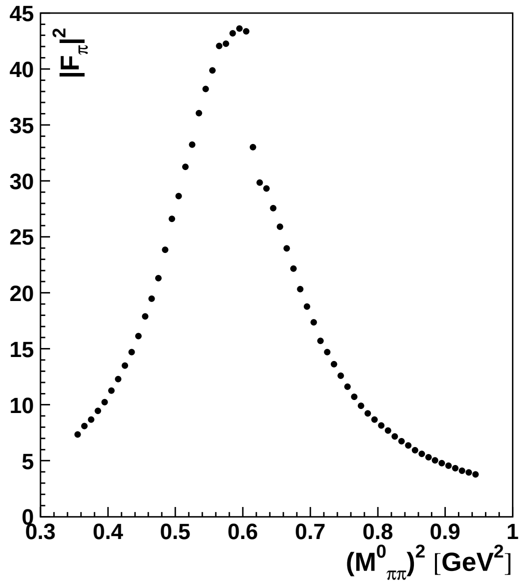

Figure 43: $|F_\pi|^2$ as a function of $(M^0_{\pi\pi})^2$.

undressed from pionic final state radiation) is shown.

7 Evaluation of $\Delta^{\pi\pi} a_\mu$

The dispersive integral for $\Delta^{\pi\pi} a_\mu$ is computed as the sum of the values for $\sigma^0_{\pi\pi}$ listed in Table 5 times the kernel $K(s)$:

$$\Delta^{\pi\pi} a_\mu = \frac{1}{4\pi^3} \int_{s_{min}}^{s_{max}} \mathrm{d}s\, \sigma^0_{\pi\pi(\gamma)}(s)\, K(s) \ , \tag{7.1}$$

where the kernel, see the second paper of Ref. [5], is given by

$$K(s) = x^2\Big(1 - \frac{x^2}{2}\Big) + (1+x)^2(1+x^{-2})\Big(\log(1+x) - x + \frac{x^2}{2}\Big) + \frac{1+x}{1-x} x^2 \log x$$

with

$$x = \frac{1 - \sqrt{1 - 4m_\mu^2/s}}{1 + \sqrt{1 - 4m_\mu^2/s}}$$

Eq. 7.1 gives

$$\Delta^{\pi\pi} a_\mu = (387.2 \pm 0.5_{\rm stat} \pm 2.4_{\rm exp} \pm 2.3_{\rm th}) \times 10^{-10}$$

in the interval 0.35$< M^2_{\pi\pi} <$ 0.95 GeV^2. Contributions to the systematic errors on $\Delta^{\pi\pi} a_\mu$ are given in Table 9.

$M^2_{\pi\pi}\|(M^0_{\pi\pi})^2$ GeV^2	$\sigma_{\pi\pi\gamma}$ nb/GeV^2	$\sigma^{bare}_{\pi\pi}$ nb	$\|F(\pi)\|^2$	$M^2_{\pi\pi}\|(M^0_{\pi\pi})^2$ GeV^2	$\sigma_{\pi\pi\gamma}$ nb/GeV^2	$\sigma^{bare}_{\pi\pi}$ nb	$\|F(\pi)\|^2$
0.355	13.07±0.16±0.09	309±4	7.35±0.11	0.655	59.62±0.19±0.31	683.8±2.7	25.90±0.10
0.365	14.21±0.16±0.09	335±4	8.09±0.11	0.665	56.28±0.18±0.29	626.9±2.5	23.98±0.10
0.375	15.20±0.16±0.10	354±4	8.68±0.11	0.675	53.43±0.18±0.28	573.5±2.4	22.16±0.09
0.385	16.60±0.16±0.11	380±4	9.45±0.11	0.685	49.84±0.17±0.26	520.8±2.2	20.33±0.09
0.395	18.23±0.17±0.11	405±4	10.23±0.11	0.695	47.22±0.16±0.24	476.0±2.0	18.78±0.08
0.405	19.97±0.16±0.12	439±4	11.28±0.11	0.705	44.65±0.16±0.23	435.8±1.9	17.38±0.08
0.415	22.00±0.17±0.14	472±4	12.30±0.11	0.715	41.40±0.15±0.21	389.5±1.7	15.70±0.07
0.425	24.09±0.17±0.15	511±4	13.51±0.11	0.725	39.40±0.14±0.20	360.7±1.6	14.69±0.07
0.435	26.57±0.17±0.16	548±4	14.70±0.11	0.735	37.80±0.14±0.19	331.1±1.5	13.63±0.06
0.445	29.26±0.18±0.17	592±4	16.13±0.12	0.745	36.05±0.14±0.18	302.6±1.4	12.60±0.06
0.455	32.56±0.19±0.19	648±4	17.91±0.12	0.755	34.13±0.13±0.17	276.0±1.3	11.63±0.05
0.465	35.60±0.19±0.20	695±4	19.49±0.12	0.765	32.50±0.13±0.16	251.4±1.2	10.70±0.05
0.475	39.18±0.19±0.22	749±4	21.31±0.13	0.775	31.14±0.12±0.16	230.2±1.1	9.91±0.05
0.485	44.28±0.20±0.25	826±5	23.85±0.13	0.785	30.01±0.12±0.15	212.3±1.0	9.24±0.04
0.495	49.73±0.21±0.28	908±5	26.61±0.14	0.795	29.23±0.11±0.15	197.4±0.9	8.68±0.04
0.505	54.17±0.22±0.30	963±5	28.65±0.14	0.805	28.46±0.11±0.14	183.7±0.9	8.16±0.04
0.515	59.20±0.22±0.33	1035±5	31.25±0.15	0.815	27.79±0.11±0.14	171.3±0.8	7.69±0.04
0.525	63.90±0.23±0.35	1085±5	33.25±0.15	0.825	27.06±0.11±0.14	158.4±0.8	7.180±0.035
0.535	69.82±0.24±0.38	1158±5	36.05±0.16	0.835	26.43±0.10±0.13	147.0±0.7	6.732±0.032
0.545	74.68±0.24±0.41	1209±5	38.22±0.16	0.845	26.02±0.10±0.13	137.5±0.6	6.358±0.030
0.555	79.20±0.24±0.43	1242±5	39.88±0.16	0.855	25.63±0.10±0.13	127.4±0.6	5.948±0.028
0.565	83.79±0.25±0.45	1289±5	42.06±0.16	0.865	25.43±0.10±0.13	119.2±0.6	5.621±0.026
0.575	85.79±0.25±0.46	1276±5	42.27±0.16	0.875	25.49±0.10±0.13	111.5±0.5	5.304±0.025
0.585	88.66±0.25±0.58	1285±5	43.18±0.16	0.885	25.49±0.10±0.13	104.9±0.5	5.038±0.023
0.595	90.24±0.25±0.55	1282±5	43.61±0.16	0.895	25.77±0.10±0.13	98.7±0.4	4.784±0.022
0.605	91.38±0.25±2.01	1262±5	43.37±0.16	0.905	26.20±0.10±0.13	93.1±0.4	4.550±0.020
0.615	70.10±0.21±2.83	898.1±3.5	33.03±0.13	0.915	26.81±0.10±0.13	87.6±0.4	4.322±0.019
0.625	65.02±0.20±0.43	801.7±3.2	29.84±0.12	0.925	27.49±0.10±0.14	82.8±0.4	4.117±0.018
0.635	64.92±0.20±0.34	785.7±3.1	29.31±0.12	0.935	28.57±0.10±0.14	78.74±0.33	3.950±0.017
0.645	62.40±0.20±0.32	734.2±2.9	27.57±0.11	0.945	29.86±0.10±0.15	74.74±0.31	3.780±0.016

Table 8: $\sigma_{\pi\pi\gamma}$, $\sigma^{bare}_{\pi\pi}$ cross sections and pion form factor $|F_\pi|^2$ for bins of 0.01 GeV^2, where the value given indicates the bin center. While the $\sigma_{\pi\pi\gamma}$ cross section is given as a function of $M^2_{\pi\pi}$, the $\sigma^{bare}_{\pi\pi}$ cross section and $|F^2_\pi|$ are given as function of $(M^0_{\pi\pi})^2$. The error attached to each value represents the statistical uncertainty. For $\sigma_{\pi\pi\gamma}$, the second error gives the systematic uncertainty obtained by adding the contributions listed in Table 7 quadratically for each value of 0.01 GeV^2.

Reconstruction Filter	negligible
Background subtraction	0.3 %
Trackmass	0.2 %
Particle ID	negligible
Tracking	0.3 %
Trigger	0.1 %
Unfolding	negligible
Acceptance ($\theta_{\pi\pi}$)	0.2 %
Acceptance (θ_{π})	negligible
Software Trigger (L3)	0.1 %
Luminosity ($0.1_{th} \oplus 0.3_{exp}$)%	0.3 %
$\sqrt{s}$ dep. of H	0.2 %
Total exp systematics	0.6 %
Vacuum Polarization	0.1 %
FSR resummation	0.3 %
Rad. function H	0.5 %
Total theory systematics	0.6 %

Table 9: List of systematic errors on $\Delta^{\pi\pi} a_\mu$

8 Comparison between 2008 and 2005 analyses

In order to compare consistently the $\pi^+\pi^-\gamma$ differential cross section from this analysis to that from our previous analysis, two corrections have been applied to the previous results:

- a -0.7% overall shift, due to the new evaluation of the Bhabha cross section, obtained from the updated version of the Babayaga generator (see Sec. 4.11);
- an energy-dependent effect due to a double counting of the calorimeter cluster efficiency in the evaluation of the trigger correction, which overestimates the cross section mainly at low-mass values by a few percent.

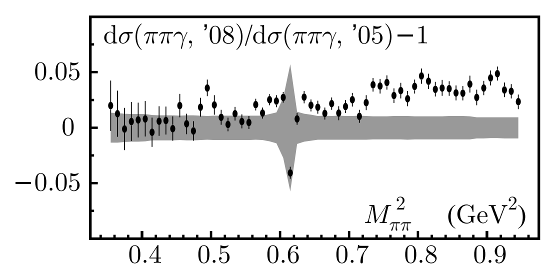

Figure 44: Comparison of the present result with the published data, updated for the effects described in the text. The band is just the fractional systematic error of the ratio.

As a result of these updates, the value of $\Delta^{\pi\pi} a_\mu$ from our previous analysis changes to $(384.4 \pm\ 0.8_{\rm stat} \pm\ 4.6_{\rm sys}) \times 10^{-10}$. The fractional difference between the spectra for the present analysis and that previously published (with updates), is shown in Fig. 44. While the agreement below the ρ peak is good, above 0.7 GeV^2 there is some difference between the two spectra. The value obtained for the integral is consistent between the two data sets (as shown in Table 10). Because of the analysis improvements and the quality of the 2002 data, we consider that the present results to supersede those previously published.

$\Delta^{\pi\pi}a_\mu\times 10^{10}$	$0.35 < M^2_{\pi\pi} < 0.95\,\mathrm{GeV}^2$
published 05	$388.7 \pm\ 0.8_{\mathrm{stat}} \pm\ 4.9_{\mathrm{sys}}$
updated 05	$384.4 \pm\ 0.8_{\mathrm{stat}} \pm\ 4.6_{\mathrm{sys}}$
new data 08	$387.2 \pm\ 0.5_{\mathrm{stat}} \pm\ 3.3_{\mathrm{sys}}$

Table 10: Comparison among $\Delta^{\pi\pi}a_\mu$ values from KLOE analyses.

9 Comparison with CMD-2 and SND results

We may compare the present result on $|F_\pi|^2$ with the results from the energy scan experiments at Novosibirsk CMD-2 [39] and SND [40]. For a given energy scan experiment, whenever there are several data points falling in one $0.01\,\mathrm{GeV}^2$ bin, we average the values. The result can be seen in Fig. 45, left. Fig. 45, right, shows the fractional difference between the data points from the energy scan experiments (CMD-2 and SND) and the KLOE data. There is reasonable agreement between the experiments, as also indicated by the

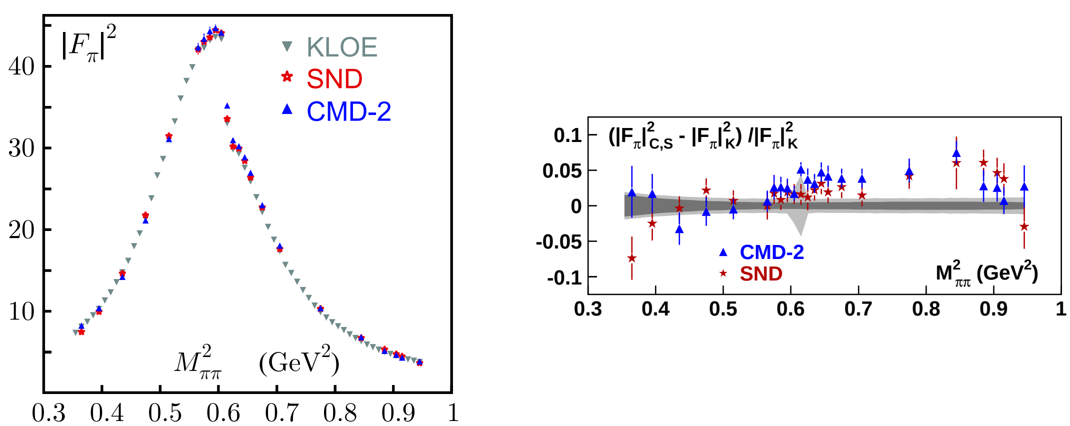

Figure 45: Left. $|F_\pi|^2$ from CMD-2 [39], SND [40] and KLOE with statistical errors. Right. Fractional difference between CMD-2 (C) or SND (S) and the KLOE (K) results. The dark (light) band is the KLOE statistical (statistical $\oplus$ systematic) error. For CMD-2 and SND points the statistical$\oplus$systematic error is shown.

computed values of $\Delta^{\pi\pi}a_\mu$ given below in the range of overlap $0.630 < M_{\pi\pi} < 0.958\,\mathrm{GeV}$, combining statistical and systematic errors in quadrature:

$$\begin{aligned} \text{SND, 2006 [40]} \quad & \Delta^{\pi\pi}a_\mu = (361.0 \pm 5.1)\times 10^{-10} \\ \text{CMD-2, 2007 [39]} \quad & \Delta^{\pi\pi}a_\mu = (361.5 \pm 3.4)\times 10^{-10} \\ \text{this work} \quad & \Delta^{\pi\pi}a_\mu = (356.7 \pm 3.1)\times 10^{-10}. \end{aligned}$$

A fit for the best value gives 359.2±2.1 with χ^2/dof=1.24/2, corresponding to a confidence level of 54%.

10 Conclusions

We have measured the dipion contribution to the muon anomaly, $\Delta^{\pi\pi}a_\mu$, in the interval $0.592 < M_{\pi\pi} < 0.975$ GeV, with negligible statistical error and a 0.6% experimental systematic uncertainty. Radiative corrections calculations increase the systematic uncertainty to 0.9%. Combining all errors we find:

$$\Delta^{\pi\pi}a_\mu(0.592 < M_{\pi\pi} < 0.975 \text{ GeV}) = (387.2 \pm 3.3) \times 10^{-10}.$$

This result is consistent with our previous value, with a total error smaller by 30%. Our new result confirms the current disagreement between the standard model prediction for a_μ and the measured value.

Acknowledgements

We would like to thank Carlo Michel Carloni Calame, Henryk Czyż, Agnieszka Grzelińska, Fred Jegerlehner, Johann Kühn, Guido Montagna, Germán Rodrigo and Olga Shekhovtsova for numerous useful discussions. We also would like to thank our referees, Cesare Bini, Juliet Lee-Franzini and Matthew Moulson, for countless stimulating input.

A Results of the background fit procedure

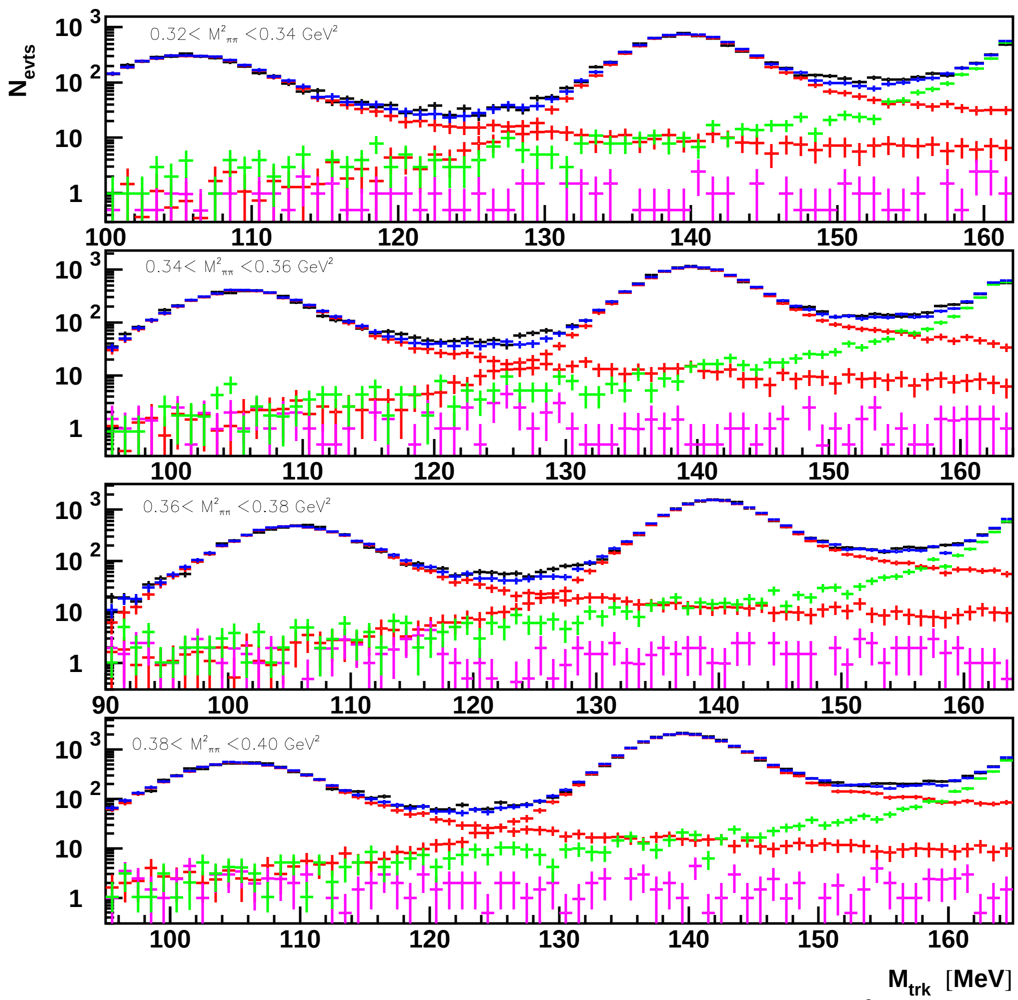

Figure 46: Results of the background fit procedure for slices in $M^2_{\pi\pi}$ between 0.32 and 0.40 GeV^2. Shown are the data (black), sum of all Monte Carlo contributions (blue), $\pi\pi\gamma(\gamma)$ and $\mu\mu\gamma(\gamma)$ Monte Carlo (red), $\pi\pi\pi$ Monte Carlo (green) and Bhabha Monte Carlo (magenta).

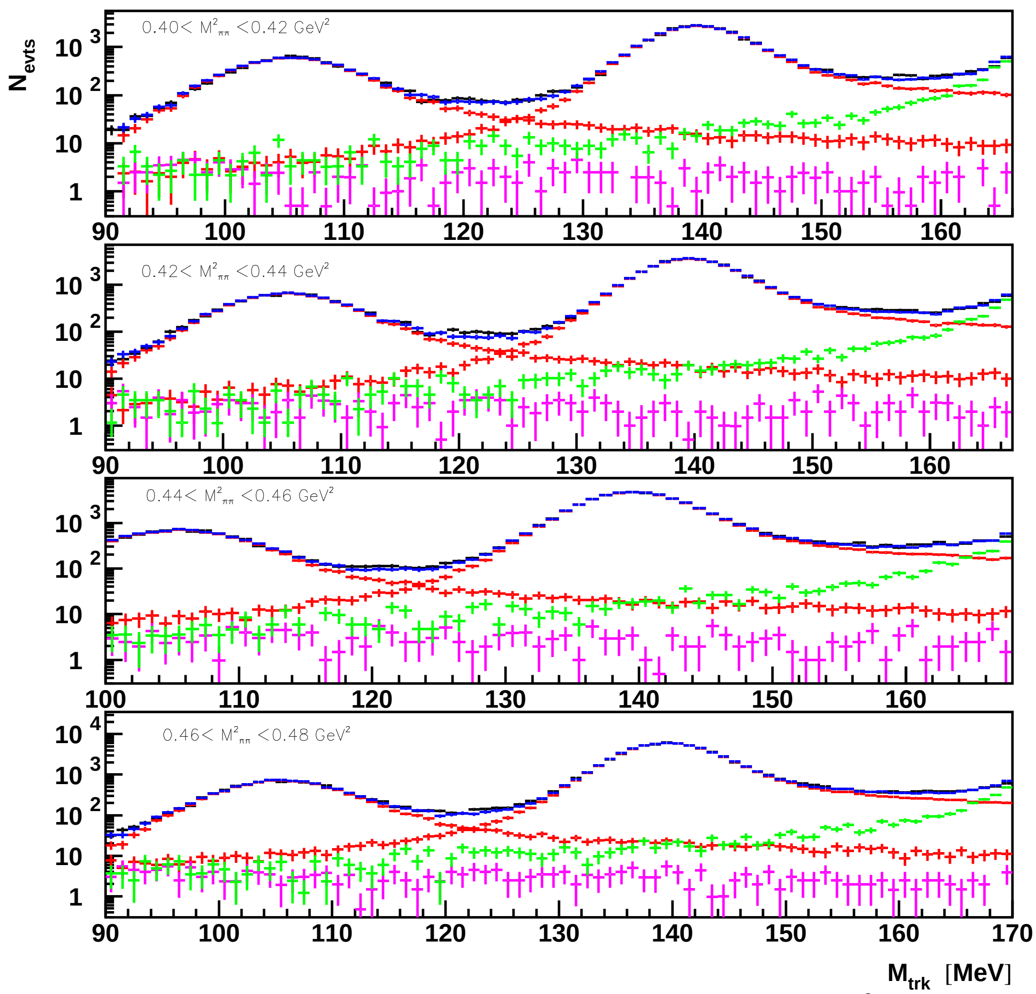

Figure 47: Results of the background fit procedure for slices in $M^2_{\pi\pi}$ between 0.40 and 0.48 GeV^2. Shown are the data (black), sum of all Monte Carlo contributions (blue), $\pi\pi\gamma(\gamma)$ and $\mu\mu\gamma(\gamma)$ Monte Carlo (red), $\pi\pi\pi$ Monte Carlo (green) and Bhabha Monte Carlo (magenta).

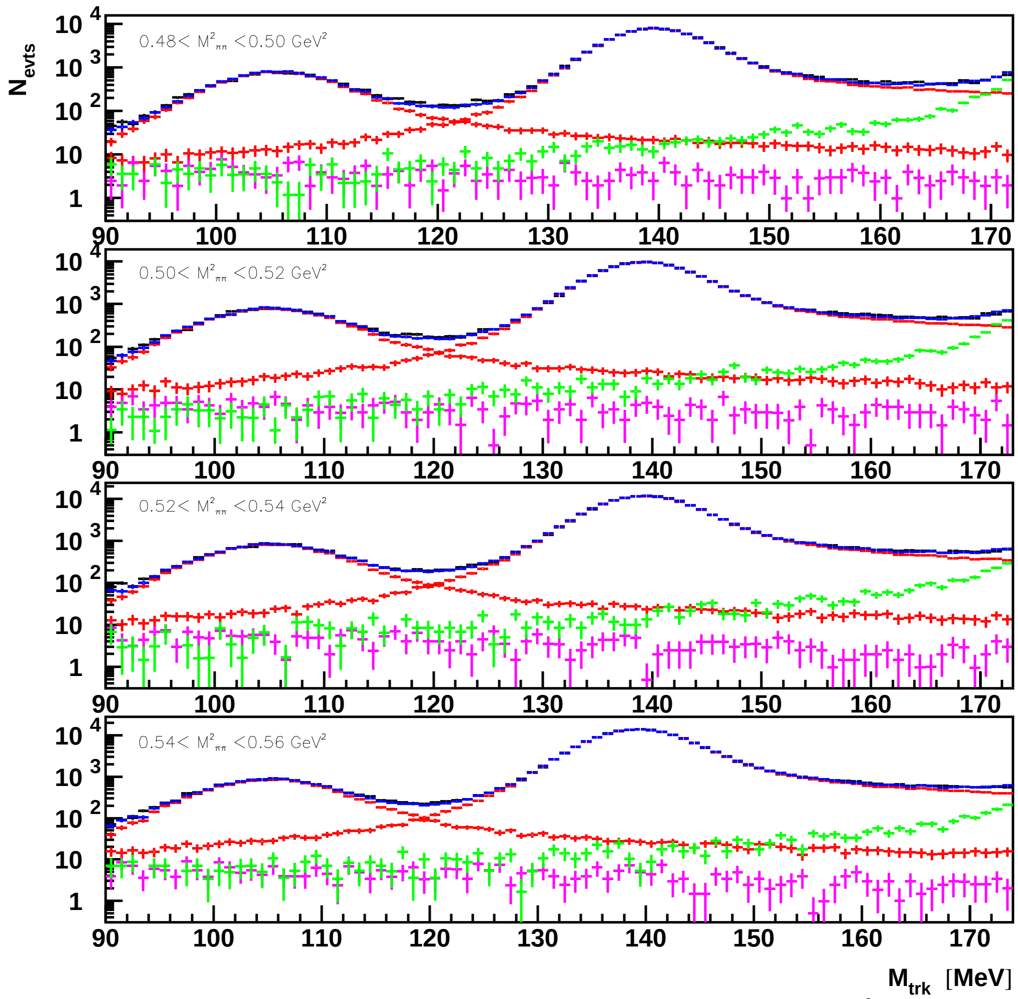

Figure 48: Results of the background fit procedure for slices in $M_{\pi\pi}^2$ between 0.48 and 0.52 GeV^2. Shown are the data (black), sum of all Monte Carlo contributions (blue), $\pi\pi\gamma(\gamma)$ and $\mu\mu\gamma(\gamma)$ Monte Carlo (red), $\pi\pi\pi$ Monte Carlo (green) and Bhabha Monte Carlo (magenta).

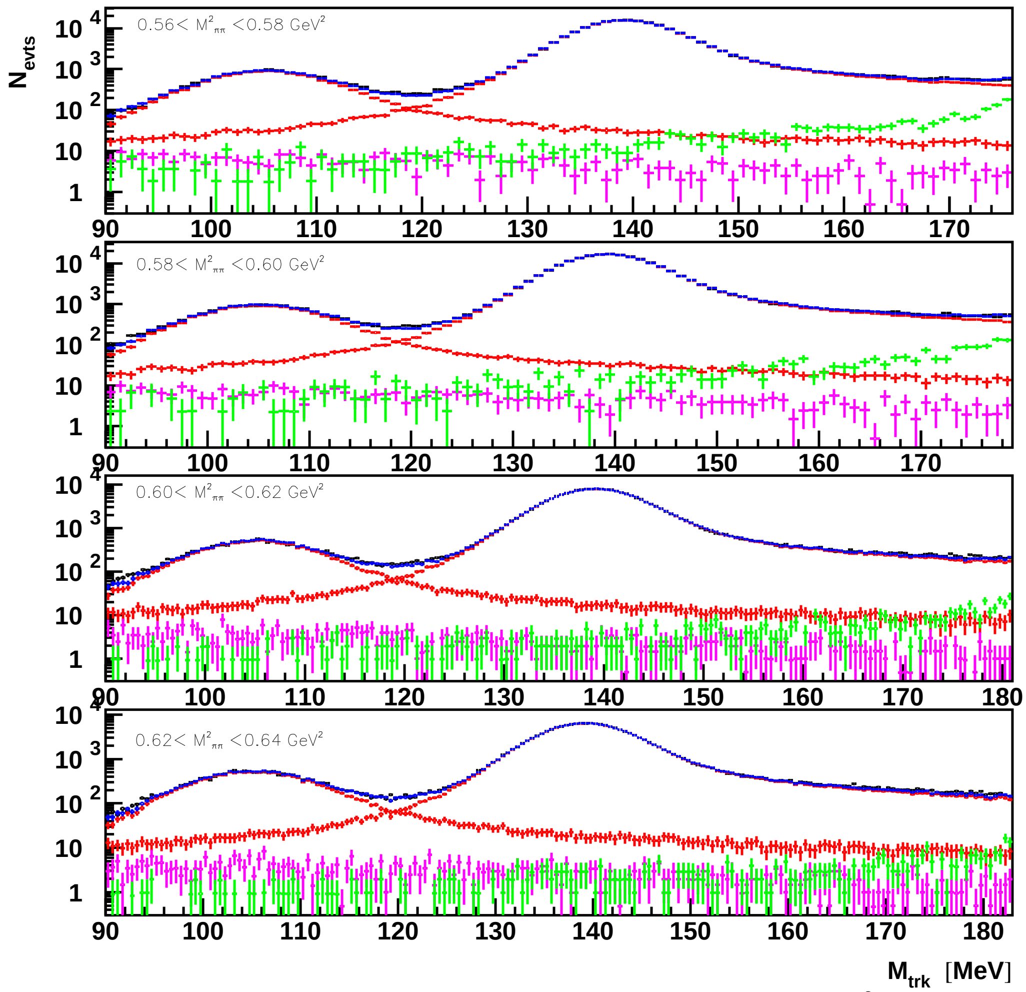

Figure 49: Results of the background fit procedure for slices in $M^2_{\pi\pi}$ between 0.56 and 0.64 GeV^2. Shown are the data (black), sum of all Monte Carlo contributions (blue), $\pi\pi\gamma(\gamma)$ and $\mu\mu\gamma(\gamma)$ Monte Carlo (red), $\pi\pi\pi$ Monte Carlo (green) and Bhabha Monte Carlo (magenta).

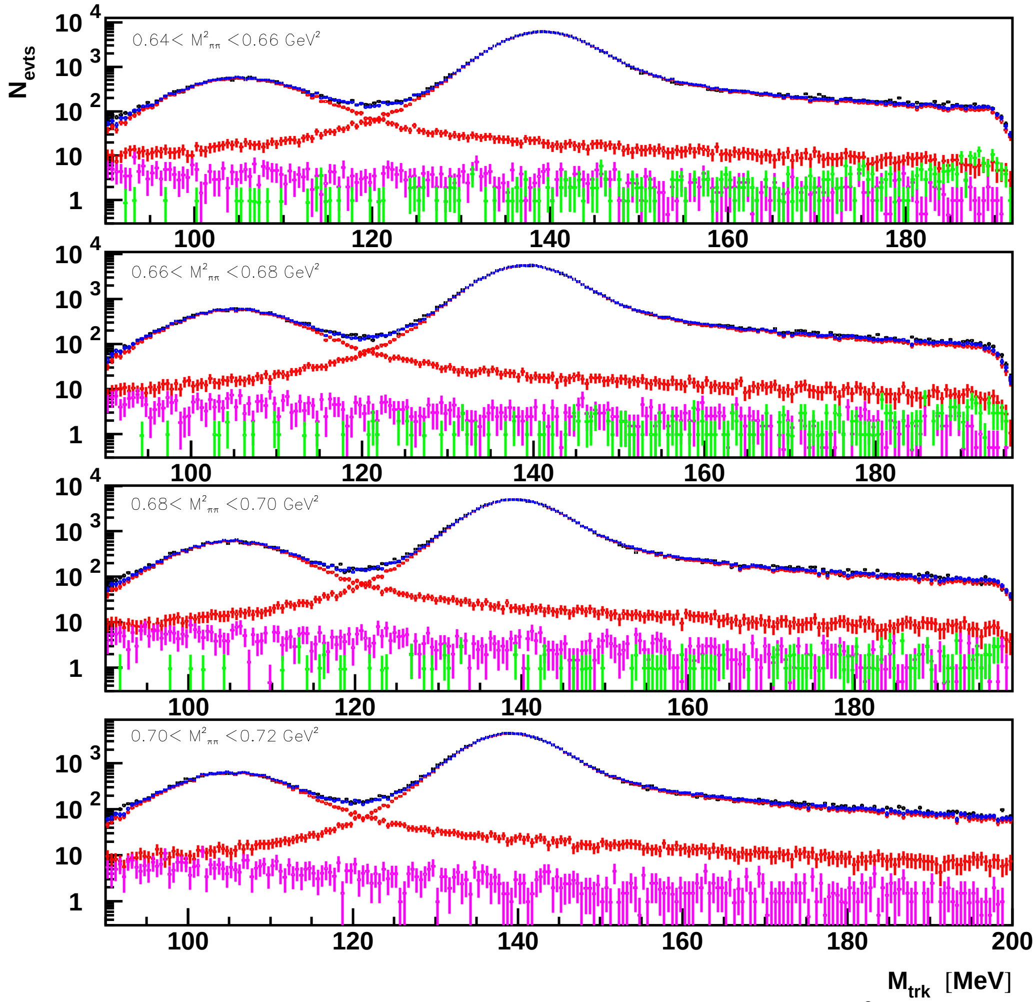

Figure 50: Results of the background fit procedure for slices in $M^2_{\pi\pi}$ between 0.64 and 0.72 GeV^2. Shown are the data (black), sum of all Monte Carlo contributions (blue), $\pi\pi\gamma(\gamma)$ and $\mu\mu\gamma(\gamma)$ Monte Carlo (red), $\pi\pi\pi$ Monte Carlo (green) and Bhabha Monte Carlo (magenta).

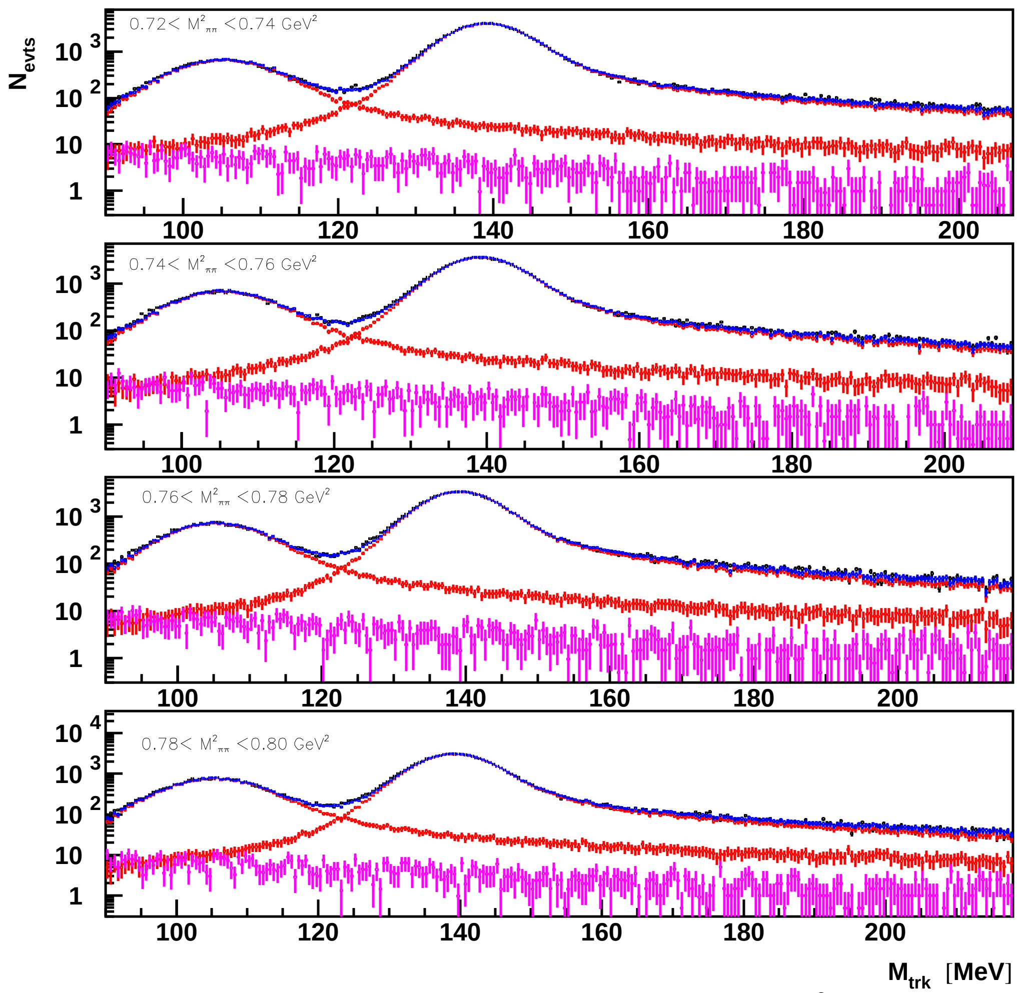

Figure 51: Results of the background fit procedure for slices in $M^2_{\pi\pi}$ between 0.72 and 0.80 GeV^2. Shown are the data (black), sum of all Monte Carlo contributions (blue), $\pi\pi\gamma(\gamma)$ and $\mu\mu\gamma(\gamma)$ Monte Carlo (red) and Bhabha Monte Carlo (magenta).

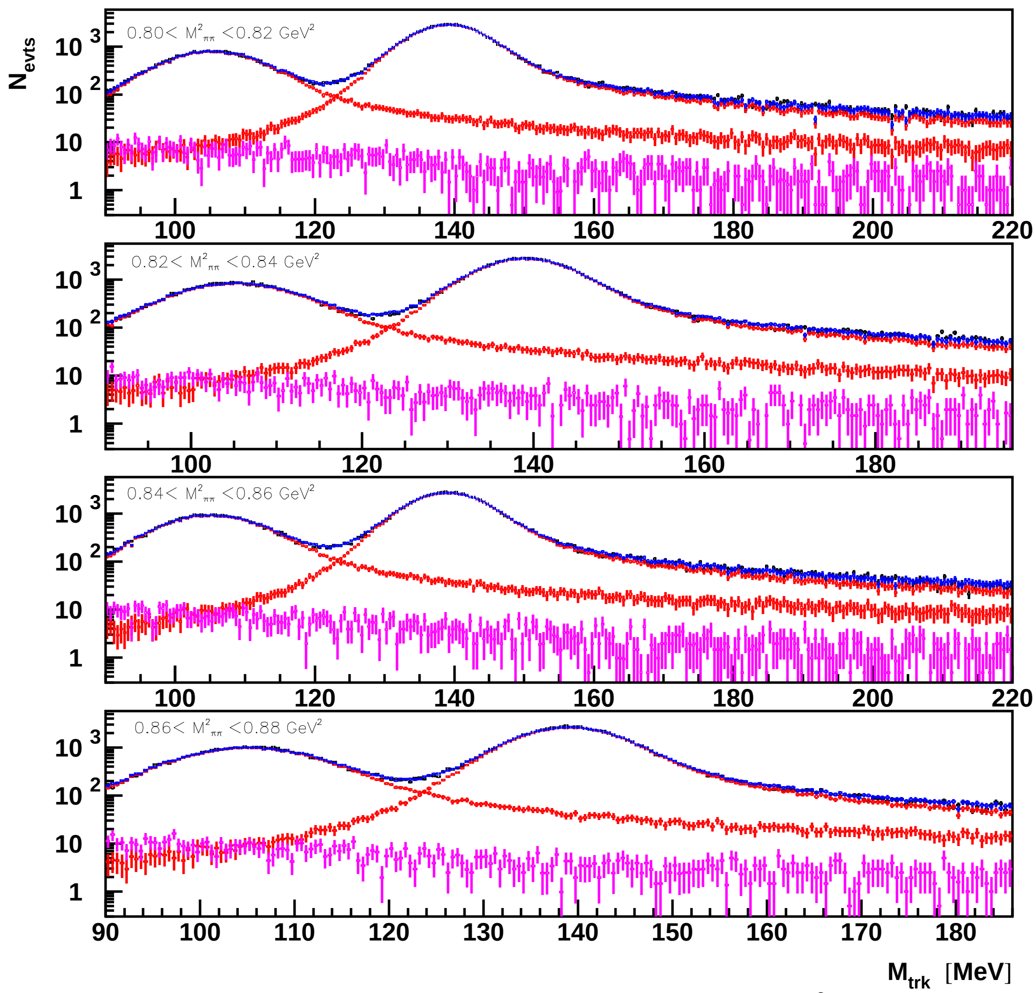

Figure 52: Results of the background fit procedure for slices in $M_{\pi\pi}^2$ between 0.80 and 0.88 GeV^2. Shown are the data (black), sum of all Monte Carlo contributions (blue), $\pi\pi\gamma(\gamma)$ and $\mu\mu\gamma(\gamma)$ Monte Carlo (red) and Bhabha Monte Carlo (magenta).

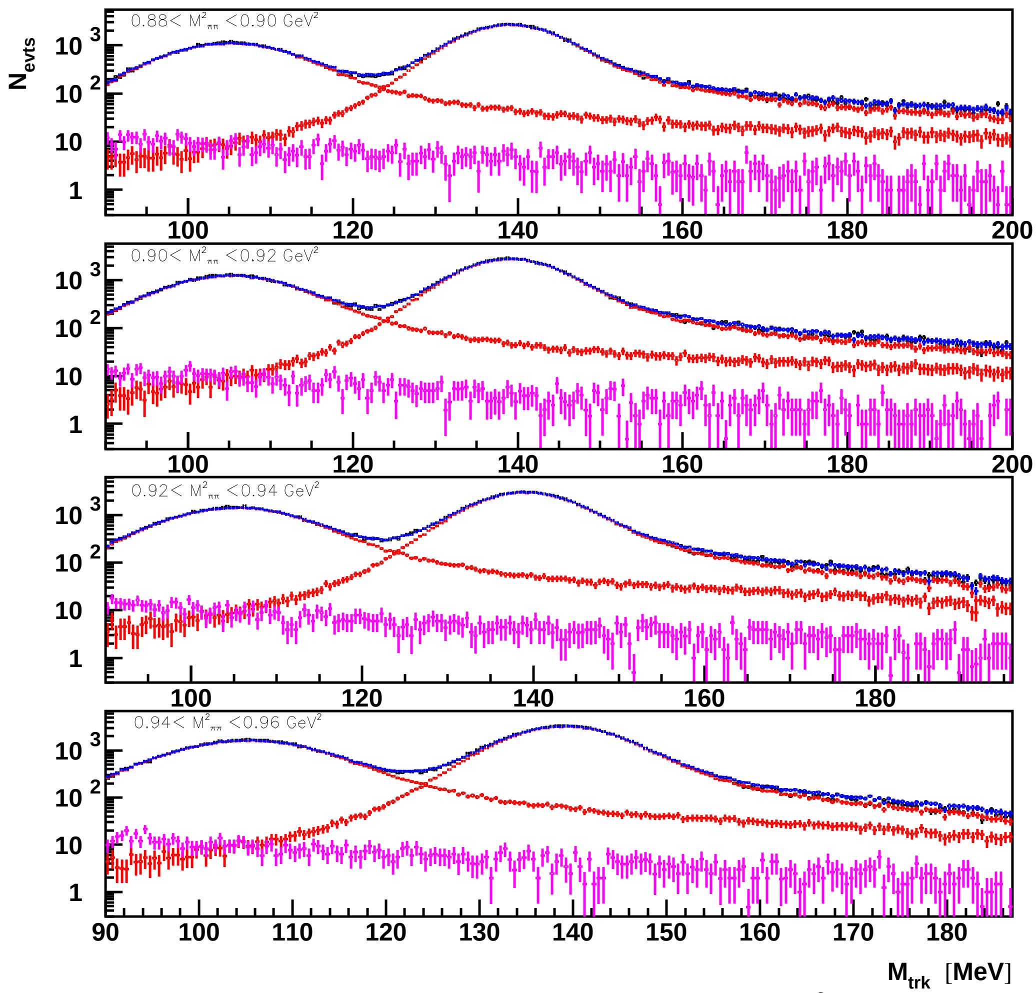

Figure 53: Results of the background fit procedure for slices in $M^2_{\pi\pi}$ between 0.88 and 0.96 GeV^2. Shown are the data (black), sum of all Monte Carlo contributions (blue), $\pi\pi\gamma(\gamma)$ and $\mu\mu\gamma(\gamma)$ Monte Carlo (red) and Bhabha Monte Carlo (magenta).

B Correcting Monte Carlo distributions

B.1 Momentum corrections

The following corrections have been applied to Monte Carlo momenta components p_i

$$p_i \quad \rightarrow \quad p_i/\zeta(\theta, s_\pi) \tag{B.1}$$

where

$$\zeta(\theta, s_\pi) = \begin{cases} c(\theta) - (1.2354 - 2.1833 s_\pi + 0.87765 s_\pi^2)10^{-3} & if\ \theta > \pi/2 \\ c(\theta) & if\ \theta < \pi/2 \end{cases}$$

and

$$c(y) = (1. - 5 \cdot 10^{-4})(1 - (y/|y|(1 - e^{-|y|/0.07}) - 1)/2.5/510)\ ;\ y = \theta - 0.85 \tag{B.2}$$

If $s_\pi > 0.8\ GeV^2$ $c \rightarrow c - 0.0002$.

If $s_\pi < 0.8\ GeV^2$ the momenta of the positive (p_i^+) and negative track (p_i^-) are smeared ($p_i^{+,-} \rightarrow p^{+,-} \cdot smear_{+,-}$) according to

$$smear_+ = \begin{cases} 1 - 0.007x & 1/20\ of\ the\ events \\ 1 - 0.0018x & else \end{cases}$$

$$smear_- = \begin{cases} 1 - 0.007x & 1/20\ of\ the\ events \\ 1 - 0.0023x & else \end{cases}$$

where x is a random Gaussian variable (with mean 0 and sigma 1). Plots on the effect of these corrections on data-MC comparison for variables of significant interest can be found in [18].

B.2 Momentum corrections for data and Monte Carlo

A second description of corrections to Monte Carlo distributions has been obtained from [41] - it acts only on the momenta of the two charged particles, not on the angles. Different from the procedure above (appendix B.1), also the momenta components of data are corrected. For the Monte Carlo distributions, corrections are identical for particles with positive and negative charge.

The data momenta get corrected in the following way:

- Positively charged track:
  - $p_{x|y}^+ = p_{x|y}^+ \times (1. - 8. \cdot 10^{-4})$
  - $p_z^+ = p_z^+ + |p_z^+| \cdot 8. \cdot 10^{-4}$
- Negatively charged track:
  - $p_{x|y}^- = p_{x|y}^- \times (1. - 2. \cdot 10^{-4})$
  - $p_z^- = p_z^- + |p_z^-| \cdot 5. \cdot 10^{-4}$

The Monte Carlo momenta get corrected in two steps:

s	δ_{VP}	s	δ_{VP}	s	δ_{VP}	s	δ_{VP}
0.355	1.0096±0.0003	0.505	1.0027±0.0004	0.655	1.0465±0.0020	0.805	1.0362±0.0012
0.365	1.0091±0.0003	0.515	1.0033±0.0003	0.665	1.0438±0.0015	0.815	1.0360±0.0012
0.375	1.0085±0.0003	0.525	1.0042±0.0003	0.675	1.0419±0.0010	0.825	1.0359±0.0012
0.385	1.0079±0.0003	0.535	1.0056±0.0003	0.685	1.0404±0.0006	0.835	1.0357±0.0012
0.395	1.0073±0.0003	0.545	1.0074±0.0002	0.695	1.0392±0.0003	0.845	1.0353±0.0012
0.405	1.0067±0.0003	0.555	1.0094±0.0002	0.705	1.0382±0.0004	0.855	1.0353±0.0012
0.415	1.0061±0.0003	0.565	1.0116±0.0003	0.715	1.0374±0.0007	0.865	1.0348±0.0012
0.425	1.0054±0.0004	0.575	1.0134±0.0004	0.725	1.0366±0.0009	0.875	1.0344±0.0012
0.435	1.0048±0.0004	0.585	1.0144±0.0006	0.735	1.0362±0.0011	0.885	1.0339±0.0012
0.445	1.0042±0.0004	0.595	1.0132±0.0006	0.745	1.0364±0.0011	0.895	1.0333±0.0012
0.455	1.0036±0.0004	0.605	1.0106±0.0009	0.755	1.0366±0.0011	0.905	1.0327±0.0012
0.465	1.0031±0.0004	0.615	1.0679±0.0007	0.765	1.0366±0.0011	0.915	1.0320±0.0012
0.475	1.0027±0.0004	0.625	1.0674±0.0045	0.775	1.0365±0.0011	0.925	1.0311±0.0012
0.485	1.0025±0.0004	0.635	1.0564±0.0035	0.785	1.0365±0.0011	0.935	1.0301±0.0012
0.495	1.0025±0.0004	0.645	1.0503±0.0027	0.795	1.0364±0.0012	0.945	1.0290±0.0012

Table 11: Vacuum Polarization values used in the analysis, see [36]. The value of s corresponds to the bin center.

1. Shifting the momenta components
   - For $s < 0.5$ GeV^2: $p_{x|y|z} = p_{x|y|z} \times (1. + 3.8 \cdot 10^{-4})$
   - For $s \geq 0.5$ GeV^2 and $s < 0.8$ GeV^2: $p_{x|y|z} = p_{x|y|z} \times (1. + 2.5 \cdot 10^{-4})$
   - For $s \geq 0.8$ GeV^2: $p_{x|y|z} = p_{x|y|z} \times (1. + 3.0 \cdot 10^{-4})$
2. Smearing the momenta components

   If $s_\pi < 0.7\ GeV^2$ the momenta of the positive (p_i^+) and negative track (p_i^-) are smeared ($p_i^{+,-} \rightarrow p^{+,-} \cdot smear_{+,-}$) according to

   $$smear_{+,-} = \begin{cases} 1 - 0.005x & 1/20\ of\ the\ events \\ 1 - 0.0015x & else \end{cases}$$

   If $s_\pi \geq 0.7\ GeV^2$ the momenta of the positive (p_i^+) and negative track (p_i^-) are smeared ($p_i^{+,-} \rightarrow p^{+,-} \cdot smear_{+,-}$) according to

   $$smear_{+,-} = \begin{cases} 1 - 0.007x & 1/20\ of\ the\ events \\ 1 - 0.0018x & else \end{cases}$$

   where x is a random Gaussian variable (with mean 0 and sigma 1).

C Vacuum Polarization

Table 11 shows the values used for δ_{VP} to obtain the *bare* cross section (see Sec. 5.3). The values are taken from [36].

References

[1] G. W. Bennett *et al.* [Muon G-2 Collaboration], Phys. Rev. D **73** (2006) 072003

[2] J.P. Miller, E. de Rafael and B.L. Roberts, Rept. Prog. Phys. **70** (2007) 795

[3] F. Jegerlehner, [hep-ph/0703125]

[4] C. Bouchiat and L. Michel, J. Phys. Radium **22** (1961) 121.

[5] S. Brodsky and E. de Rafael, Phys. Rev. **168** (1968) 1620; B.E. Lautrup and E. de Rafael, Nuovo Cimento, **1A** (1971) 238.

[6] A. Aloisio *et al.* [KLOE coll.], Phys. Lett. B **606** (2005) 12

[7] F. Ambrosino *et al.* [KLOE coll.], Nucl. Instrum. Meth. A **534** (2004) 403.

[8] S. Binner, J. H. Kühn and K. Melnikov, Phys. Lett. B 459 (1999) 279

[9] F. Bossi, M. Moulson, M. Palutan, B. Sciascia, KLOE Memo 281

[10] M. Adinolfi *et al.* [KLOE coll.], Nucl. Instrum. Meth. A **492** (2002) 134

[11] B. Valeriani, KLOE Memo 295

[12] S.Müller, KLOE Memo 287

[13] M. Moulson, S.Müller, KLOE Memo 288

[14] F. Nguyen, KLOE Memo 294

[15] R. Brun *et al.*, CERN Program Library Y250 (1995)

[16] R. Barlow, C. Beeston, Comp. Phys. Comm. 77 (1993) 219

[17] S. Baker, D. Cousins, Nucl. Inst. Meth. 221 (1984) 437

[18] B. Valeriani, G. Venanzoni, KLOE Memo 291

[19] H. Czyż, E. Nowak, Acta Phys. Polon. B34 (2003) 5231

[20] H. Czyż, E. Nowak-Kubat, Phys. Lett. B634 (2006) 493

[21] F. A. Berends, C. G. Papadopoulos, R. Pittau, Comput. Phys. Commun. 136 (2001) 148

[22] O. Shekhovtsova, private communication. See also G. Pancheri, O. Shekhovtsova and G. Venanzoni, J. Exp. Theor. Phys. **106** (2008) 470

[23] F. Ambrosino , Nucl. Instrum. Meth. A **534** (2004) 403

[24] H. Czyż, private communication

[25] G. D'Agostini, Nucl. Instrum. Meth. A **362** (1995) 487

[26] G. D'Agostini: URL http://www.roma1.infn.it/ dagos/bayes_distr.txt

[27] H.Czyż *et al.*, private communication

[28] A. Denig *et al.*, KLOE Note 192 (2004)

[29] A. Denig, F. Nguyen, KLOE Note 202 (2005)

[30] F. Ambrosino *et al.* [KLOE coll.], Eur. Phys. J. C **47** (2006) 589

[31] C. M. Carloni Calame *et al.*, Nucl. Phys. B **584** (2000) 459

[32] G. Balossini *et al.*, Nucl. Phys. B **758** (2006) 227

[33] H. Czyż, A. Grzelińska,, J. Kühn, G. Rodrigo, Eur. Phys. J. C 27 (2003), 563

[34] F. Jegerlehner, Springer Tracts in Mod. Phys., 226 (2007)

[35] A. Höfer, J. Gluza and F. Jegerlehner, Eur. Phys. J. C **24** (2002) 51

[36] $\Delta\alpha_{had}(s)$ points have been provided by Fred Jegerlehner. URL http://www-com.physik.hu-berlin.de/˜fjeger/alphaQEDn.uu

[37] J.S. Schwinger, *Particles, Sources and Fields, Vol.3*, Redwood City, USA Addison-Wesley (1989) 99

[38] The covariance matrix can be retrieved from the following web page:
URL http://www.lnf.infn.it/kloe/ppg/

[39] R. R. Akhmetshin *et al.* [CMD-2 coll.], Phys. Lett. B **648** (2007) 28

[40] M. N. Achasov *et al.*, [SND coll.], J. Exp. Theor. Phys. **103** (2006) 380

[41] P. Beltrame, private communication